

Review

Recent Advances in the Reverse Water–Gas Conversion Reaction

Changjian Zhou ^{1,†} , Jiahao Zhang ^{1,†}, Yuqing Fu ¹ and Hui Dai ^{2,*}

¹ School of Chemistry and Chemical Engineering, Yancheng Institute of Technology, Yancheng 224051, China; zcj@ycit.cn (C.Z.)

² College of Materials and Chemistry & Chemical Engineering, Chengdu University of Technology, Chengdu 610059, China

* Correspondence: daihui18@cdut.edu.cn

† These authors contributed equally to this work.

Abstract: The increase in carbon dioxide emissions has significantly impacted human society and the global environment. As carbon dioxide is the most abundant and cheap C1 resource, the conversion and utilization of carbon dioxide have received extensive attention from researchers. Among the many carbon dioxide conversion and utilization methods, the reverse water–gas conversion (RWGS) reaction is considered one of the most effective. This review discusses the research progress made in RWGS with various heterogeneous metal catalyst types, covering topics such as catalyst performance, thermodynamic analysis, kinetics and reaction mechanisms, and catalyst design and preparation, and suggests future research on RWGS heterogeneous catalysts.

Keywords: CO₂ conversion; CO; reverse water–gas conversion reaction; catalyst design



Citation: Zhou, C.; Zhang, J.; Fu, Y.; Dai, H. Recent Advances in the Reverse Water–Gas Conversion Reaction. *Molecules* **2023**, *28*, 7657. <https://doi.org/10.3390/molecules28227657>

Academic Editor: Margarita D. Popova

Received: 16 October 2023

Revised: 7 November 2023

Accepted: 16 November 2023

Published: 18 November 2023



Copyright: © 2023 by the authors. Licensee MDPI, Basel, Switzerland. This article is an open access article distributed under the terms and conditions of the Creative Commons Attribution (CC BY) license (<https://creativecommons.org/licenses/by/4.0/>).

1. Introduction

With the development of industry and human activities, the concentration of carbon dioxide (CO₂) in the global atmosphere is increasing yearly. As the main component of greenhouse gases, the CO₂ concentration in the atmosphere continues to rise, causing a series of severe environmental problems such as climate warming, glacier melting, and ocean acidification, seriously threatening the living environment of human beings [1].

At present, fossil fuels are still the main mode for humans to obtain primary energy, and forms of renewable energy, such as solar and wind energy, are still in the development stage and cannot yet fully replace fossil fuels. CO₂ is an abundant, inexpensive, non-toxic, non-flammable, and renewable single-carbon structural unit that can be used as a good carbon source.

In recent years, in order to cope with the negative impact of CO₂, in addition to developing new energy sources, carbon capture and storage (CCS) and carbon capture and utilization (CCU) technologies have attracted widespread attention due to their high efficiency and easy application in capturing large amounts of CO₂ [2]. CCS compresses CO₂ from the source into high-density CO₂, making it suitable for long-term transportation, storage, and monitoring, but the potential risk of leakage and continuous on-site monitoring are the main disadvantages related to this technology. Meanwhile, CCU uses different strategies to convert carbon dioxide into useful chemical products such as fuels (such as methanol) and materials (polymers) [3,4]. CCU is more useful than CCS because value-added products can be obtained using the captured CO₂. In addition, CCU also offers no possibility of carbon dioxide leakage, which makes it promising in terms of sustainability and environmental friendliness [5]. CO₂ utilization modes mainly include biological utilization, mineralization utilization, chemical synthesis, etc. In many CO₂ utilization technologies, CO₂ produces a variety of high-value basic chemicals through catalytic conversion, a process that has been widely studied by researchers. CO₂ catalytic

conversion technology mainly includes thermal catalysis [6–9], photocatalysis [10,11], electrocatalysis [12,13], and so on. The research on CO₂ catalytic conversion mainly focuses on CO₂ catalytic hydrogenation.

CO₂ catalytic conversion research focuses on CO₂ catalytic hydrogenation, a very green and environmentally friendly method for converting carbon dioxide into high-value substances such as CO, methanol, olefins, and alkanes [14,15]. According to the reaction pathway, the catalytic hydrogenation of CO₂ mainly generates CO [16,17], methane [18,19], and hydrocarbons [20,21].

In summary, whether from the perspective of protecting the environment or CO₂ utilization, the catalytic hydrogenation of CO₂ is a method with broad application prospects to reduce the greenhouse effect and provide energy resources. However, CO₂ has a very stable C=O bond and is thermodynamically difficult to activate [22]. Researchers have tried to reduce the activation energy of the CO₂ reduction reaction by adding catalysts to achieve the goal of efficient CO₂ conversion. Therefore, preparing simple and easily synthesized high-activity catalysts to convert carbon dioxide into high-value-added products is significant for improving the natural environment and addressing the energy demand.

CO₂ catalytic hydrogenation to CO is known as the reverse water–gas conversion (RWGS) reaction. The CO produced via this reaction can be used as a syngas, often used to synthesize methanol, higher alcohols, or Fischer–Tropsch fuels. This method is expected to be an effective way to achieve carbon neutrality and cycling and will significantly impact the environment and the future energy mix.

RWGS mainly converts the greenhouse gas CO₂ into CO. However, this reaction also produces the byproduct CH₄. Therefore, developing an RWGS reaction catalyst with high CO selectivity is necessary to convert CO₂ into CO in the RWGS reaction. The RWGS reaction is a typical endothermic reaction. From a thermodynamic point of view, since the RWGS reaction is endothermic, increasing the temperature during the reaction is more conducive to the equilibrium moving in a positive direction in the RWGS reaction. From a kinetic point of view, it has a higher reaction rate at a high temperature. Combined with thermodynamics and kinetics, the RWGS reaction is a process with high energy consumption [23]. At the same time, a high temperature will also lead to catalyst sintering, carbon deposition, and deactivation. Therefore, developing low-temperature, high-activity, and high-selectivity RWGS reaction catalysts has become the focus of current research, and many reviews of this work have been published [1,24–29]. Here, we review the research progress made in RWGS with different kinds of heterogeneous metal catalysts, including catalyst design and preparation, catalyst performance, thermodynamic analysis, kinetics and mechanism of reaction, etc., and predict future research on RWGS heterogeneous catalysts.

2. Results and Discussion

2.1. Reaction Mechanism of the Reverse Water–Gas Conversion Reaction

The RWGS reaction has unique advantages as one of the ways to utilize CO₂. In order to design a reasonable catalyst, it is important to understand the mechanism of CO formation in the CO₂ hydrogenation reaction in detail. The RWGS reaction's mechanism has always been a topic of debate among researchers, and existing researchers have proposed two RWGS reaction mechanisms, namely a redox mechanism (Figures 1 and 2) and an intermediate species decomposition mechanism (Figures 1 and 3). Which reaction mechanism is followed depends on the type of catalyst or reaction conditions used. The two mechanisms reported in the current literature are still controversial. It is necessary to study the reaction mechanism of various catalyst types for catalyst development.

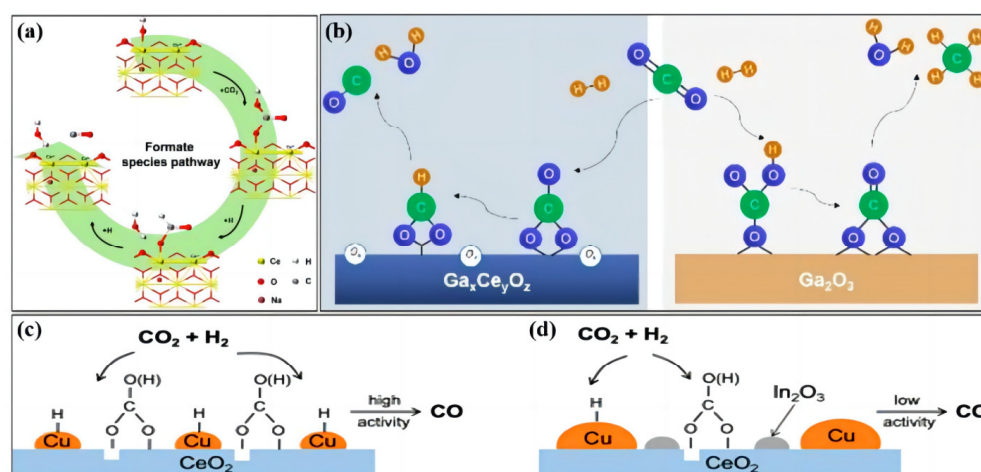
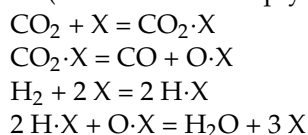


Figure 3. The associative mechanism of the RWGS reaction over (a) LN–CeO₂ (reprinted with permission from [34]. Copyright Elsevier, 2022), (b) Ga₂O₃–CeO₂ (reprinted with permission from [9]. Copyright Wiley, 2022), (c) Cu–CeO₂ (reprinted with permission from [35]. Copyright American Chemical Society, 2022), and (d) Cu₅In₅–CeO₂ (reprinted with permission from [35]. Copyright American Chemical Society, 2022).

(1) Redox mechanism

This mechanism mainly refers to the continuous oxidation and reduction of the active species in the catalyst in the CO₂ and H₂ atmosphere during the RWGS reaction to sustain the catalytic reaction. CO₂ is first adsorbed on the catalyst, combining with the active site on the catalyst surface after dissociation to produce CO. The generated active oxygen substances exist on the active site of the catalyst and then continue to reduce the catalyst to generate H₂O and release the surface active site to continue participating in the next round of the reaction. H₂ is not directly involved in the synthesis of intermediate species. In this process, CO₂ dissociation is the rate-limiting step, and the adsorption and desorption steps of CO and H₂O can be ignored. The basic reactions of the surface redox mechanism are as follows (X indicates an empty active site with no interaction with the adsorbent):



Gines and co-workers [36] prepared two catalysts, CuO/ZnO/Al₂O₃ and CuO/Al₂O₃, using the co-precipitation method. The mechanism of surface redox was proven via a kinetic experiment based on the RWGS reaction. According to the kinetic experiment results, it was found that the reaction rate of CO₂ is controlled by dissociative adsorption. The chromatographic analysis showed that only CO was formed when CO₂/N₂ was inserted, which indicated that CO₂ was dissociated from the active site on the catalyst surface to form CO. In the H₂ atmosphere, only H₂O was produced, indicating that H₂ combines with active oxygen species on the catalyst surface to form H₂O. Wang et al. [37] found that the oxygen vacancies that form on the surface of the pre-reduced Au/CeO₂ catalyst are oxidized by CO₂ to produce CO. This process corresponds to the redox mechanism of RWGS. The author also loaded Au onto different carriers and found through a pulse experiment that the amount of active oxygen on the surface of CeO₂ carriers was significantly higher than that on TiO₂ carriers. This is because CeO₂ has a good oxygen storage and supply capacity and can assist Au atoms to complete the removal and production of surface-reactive oxygen species.

(2) Decomposition mechanism of intermediate species

In the RWGS reaction, the decomposition mechanism of adsorbed intermediate species refers to CO₂ and H₂ on the catalyst, first being activated to form intermediate species and

then decomposed into CO and H₂O. In recent years, in most of the literature on RWGS reactions, formates, carbonates, and carbonyl groups were the main intermediate species formed and are considered the key steps for further CO generation.

It has been found in many research reports that there are different intermediates in RWGS reactions with different catalysts, and factors such as the properties of catalysts, the different interactions between metals and carriers, and the differences in reaction conditions lead to the complexity of the decomposition mechanism of intermediate species in RWGS reactions.

Liu et al. [38] conducted a CO₂ dissociation experiment to explore the reaction pathway. Combined with the CO₂ dissociation experiment results and temperature-programmed surface reaction, CO₂ activation can be carried out through relevant intermediate pathways. In order to further explore the active intermediate, in situ diffuse infrared Fourier transform spectroscopy (DRIFTS) is performed. After the injection of CO₂ and H₂ into the activated 15CuCe catalyst, the formate signal can be detected in addition to the carbonate signal. In the presence of H₂, the Cu atom captures the H₂ molecule, breaks the H–H bond, and then transfers the H atom to the CO₂. Formate structures are formed with the formation of C–H bonds, and these structures are manifested in the intermediates IMA3, IMA3–I, IMA4, and IMA4–I. Based on the above experimental results and density functional theory (DFT) calculation, the authors further concluded that the reaction involved the association mechanism, and the surface formates and carboxylic acid species may be important reaction intermediates. In the reaction process, a large number of surface oxygen vacancies are generated in situ and recycled, forming a synergistic catalytic effect with copper clusters, promoting the activation of CO₂ and the formation of active intermediates. The copper clusters and abundant oxygen vacancies in the 15CuCe catalyst undoubtedly create more oxygen–vacancy–active interfaces of metal clusters.

Deng et al. [39] explored the mechanism of a Cu–based slag-based geopolymer microsphere (SGS) catalyst in the RWGS reaction and conducted in situ DRIFTS experiments to observe intermediates generated during the catalytic process. The characteristic bands of bicarbonate and carbonate appeared. The formate band appeared at about 150 °C and then gradually weakened above 200 °C, indicating that formate species formed at low temperatures. The SGS is an alkaline carrier with many surface OH groups. With the increase in temperature, the OH band gradually weakened, indicating that the surface OHs participated in the catalytic process. According to DRIFTS experiment results, we observe that a gas-phase CO band appears above 250 °C, and this band becomes stronger with increasing temperature. However, no formate bands were observed above 250 °C, so it can be inferred that formate species are not intermediates in CO production. Carboxylate bands were found at 1260 cm^{−1} and 1280 cm^{−1}, so it was determined that the reaction mechanism of a Cu/SGS catalyst in the RWGS reaction is similar to the carboxylate pathway, and *COOH is the intermediate of CO₂ to CO. Combined with the results of CO₂ TPD, it can be determined that the formation of *COOH comes from the adsorption and activation of CO₂ by the abundant OH groups on the SGS carrier, where OHs on the surface of SGS react with CO₃^{2−} to form HCO₃[−]. H₂ is adsorbed on Cu to form H*, and the HCO₃[−] substance reacts with H* on the surface of Cu to form *COOH. In addition, *COOH reacts with H* on the Cu surface to form CO* and OH*, and then CO and H₂O dissociate from the Cu surface.

2.2. Overview of Catalysts of Different Systems in the Reverse Water–Gas Conversion Reaction

In industrial production, stable catalysts with high activity and selectivity need to be considered at low temperatures. However, designing a catalyst that meets all these criteria simultaneously is challenging. The current catalysts used for RWGS are mainly divided into precious metal catalysts and non-precious metal catalysts. Some representative research results are listed in Table 1.

Table 1. A brief summary of the RWGS reaction conditions of selected catalysts and their CO₂ conversion and CO selectivity.

Catalyst	Reaction Gas Ratio, H ₂ /CO ₂ /Inert Gas	Temperature °C	Reaction Airspeed mL·gcat ⁻¹ mL·h ⁻¹	CO ₂ Conversion Rate %	CO Selectivity %
Cu/CeO ₂ [37]	3:1:0	600 °C	400,000	50	100
Cu/SGS [38]	4:1:0	550 °C	3600	48	96
Pt/CeO ₂ [40]	9:9:2	500 °C	30,000	30	-
Pt _{cluster} /PN–CeO ₂ [41]	3:1:0	300 °C	12,000	17.5	99.9
Pt ₁ /SiC [32]	1:1:0	900 °C	-	54	100
Pt–Re/SiO ₂ [42]	4:1:5	400 °C	60,000	24.3	96.2
Pt/SiO ₂ [43]	1:4:5	400 °C	60,000	12.1	100
CoPd–CoO _{OV} [44]	3:1:0	300 °C	-	-	94
Ni/ZrO ₂ [45]	4:1:4	500 °C	13,500	27.6	100
Re ₂ O ₇ /SZ [46]	4:1:0	400 °C	-	18	95
Ni/Ga ₂ O ₃ [47]	4:1:5	450 °C	60,000	40	95
Fe–oxide [48]	1:1:0	600 °C	24,000	38	>85
Ni–MgO–Ce _{0.8} Zr _{0.2} O ₂ [49]	63:21:16	250 °C	50,000	4.5	90.5
Cs/Fe ₂ O ₃ [50]	4:1:0	450 °C	12,000	58	75
Cu/MnO _x [51]	12:3:5	550 °C	60,000	55.5	100
1 wt.%Cu–CeO ₂ [52]	4:1:0	600 °C	-	70	100
MoO ₃ /FAU [53]	12.5:12.5:10	500 °C	7500	15	100
Ru@MoO _{3-x} [54]	9:3:88	250 °C	100,000	45	>99
MoO ₃ /TiAlC ₂ [55]	4:1:0	550 °C	15,000	30	-
Cu–Cs–Mo ₂ C [56]	4:1:0	600 °C	12,000	-	100
Mo–P–Si ₂ O [57]	4:1:0	550 °C	12,000	18	100
Ni/CeO ₂ –Al ₂ O ₃ [58]	4:1:0	750 °C	30,000	59	94
2%Pt–CeO ₂ [59]	4:1:0	290 °C	-	27.1	100

2.3. Precious Metal Catalysts

Precious metal-supported catalysts are the most common catalysts for RWGS. The main active species are Pt, Pd, Au, Ir, Rh, Ru, etc. The main carriers are SiO₂, CeO₂, TiO₂, and Al₂O₃, on which precious metals promote the dissociation of H₂, while oxide carriers facilitate the breakage of the C=O bond in CO₂. The dispersion and chemical state of precious metal nanoparticles are the key factors affecting catalyst performance and significantly impact the adsorption behavior of reactants on the catalyst and the subsequent intermediate species transformation [40].

2.3.1. Pt–Based Catalysts

Supported Pt catalysts [32,41–43,60–63] are widely used in RWGS reactions due to their excellent H₂ dissociation and hydrogenation activity.

Chen et al. [42] found that the activation energy of CO production on a Pt/CeO₂ catalyst was significantly lower than that on a pure CeO₂ catalyst. The calculated TOF values were roughly the same across these Pt/CeO₂ catalysts, indicating that the RWGS reaction was insensitive to the size of the anchored Pt particles and the primary crystallinity of the CeO₂ carrier. The results of temperature-programmed reduction (TPR) and X-ray photoelectron spectra (XPS) showed that with the addition of Pt, the reducibility of the CeO₂ carrier was enhanced, oxygen vacancies were more easily generated, and CO₂ activation was accelerated. In addition, using in situ Fourier transform infrared spectroscopy (FT–IR) and temperature-programmed surface reaction-mass spectrometry (TPSR–MS) experiments, we found that redox and dissociation mechanisms co-exist in RWGS reactions on Pt/CeO₂ catalysts. CO₂ molecules adsorbed at the Ce³⁺ active site cannot directly generate CO, the same as the previous redox mechanism.

Liu et al. [43] prepared Pt–Re/SiO₂ catalysts with different Re contents using co-impregnation and tested the RWGS reaction. The characterization results showed that the

oxygenophilic ReO_x ($0 \leq x \leq 3.5$) near the Pt particles modified the Pt surface through partial covering and electron interaction, resulting in decreased CO adsorption sites and adsorption strength. At 400 °C, the turnover frequency of the optimal Pt–Re/SiO₂ catalyst is 3.9 times higher than that of Pt/SiO₂, and the apparent activation energy is reduced. The CO selectivity on Pt–Re/SiO₂ remains above 96.2% compared to Re/SiO₂, which produces large amounts of CH₄. The reaction order analysis showed that Pt promoted H₂ activation, while oxyphilic ReO_x enhanced CO₂ adsorption and activation. The peripheral sites of the Pt/ReO_x interface have C–O cleavage properties, which can synergistically increase RWGS activity and inhibit the production of CH₄.

To improve the potential of plasma effects on H-doped WO_y, Ge et al. [62] reported that Mo-doped Pt/WO_y (Pt/MoWO_y) significantly increases the concentration of dopant (H⁺) and oxygen vacancies in Pt/H_xMoWO_y during H₂ reduction, promoting the photothermal hydrogenation of CO₂ to CO. The developed Pt/H_xMoWO_y showed excellent catalytic performance (3.1 mmol·h^{−1}·g^{−1}) in the photothermal RWGS reaction at 140 °C, which was superior to the undoped Pt/H_xWO_y (1.02 mmol·h^{−1}·g^{−1}). The experiment and comprehensive analysis show that the abundant surface-free electrons and oxygen vacancies (VOs) in Pt/H_xMoWO_y are the reasons for the effective CO₂ adsorption and transfer. The characterization of catalysts revealed a reversible redox of Mo and W atoms during RWGS reactions, confirming that oxygen vacancies between Mo and W atoms in Pt/H_xMoWO_y act as active sites. Pt nanoparticles activate H₂ to regenerate oxygen vacancies. In addition, density functional theory calculations show that Mo doping significantly reduces the energy barrier of oxygen vacancy formation in WO_y during H₂ reduction.

He et al. [63] synthesized a single-atom catalyst, Pt₁/SiC, in which the Pt particles are uniformly dispersed on SiC and applied it in the conversion of CO₂ via the reverse water–gas shift reaction, exhibiting 100% selectivity and 54% CO₂ conversion at 900 °C with a H₂/CO₂ ratio of 1:1. It was found that in the first few hours, the Pt₁/SiC catalyst showed excellent stability with negligible decline in activity. However, over time, Pt₁/SiC was gradually deactivated. After the reaction lasted 10 h, the CO₂ conversion rate remained relatively stable at about 50%. The authors attributed the decrease in catalyst activity to two factors: the poisoning of the Pt₁/SiC catalyst caused by CO molecules and the reduction of a small amount of Pt₁/SiC.

2.3.2. Pd-Based Catalysts

Many researchers have focused on the design, preparation, and mechanism of Pd catalysts [44,64–71] based on their catalytic performance in the RWGS reaction. Here are some selected examples discussed in detail.

Nelson et al. [64] dispersed Pd on a TiO₂ carrier. The results show that in the RWGS reaction, Pd is mainly dispersed on titanium dioxide in the form of isolated atoms. Achieving atomic dispersion requires artificially increasing the absolute surface area of titanium dioxide by an order of magnitude, which can be achieved by physically mixing the catalyst Pd/TiO₂ with pure titanium dioxide prior to the RWGS reaction. Kinetic analysis, infrared spectroscopy, X-ray absorption spectroscopy, and scanning electron microscopy showed that the RWGS activity of the Pd/TiO₂–0.01 catalyst was very good within 92 h after the in situ dispersion of Pd atoms. The thermodynamic stability of Pd under high-temperature RWGS reaction conditions is related to the Pd–Ti coordination, which is related to the formation of oxygen vacancies and the artificial increase in titanium dioxide's surface area.

Onodera et al. [65] discovered that, up to 300 °C, Au-doped Pt/CeO₂ catalysts, which were created using the electroless plating method, demonstrated comparable CO₂ conversion activities to the Pt/CeO₂ catalyst. Furthermore, above 250 °C, the CO selectivity of the Au-doped Pt/CeO₂ catalysts was significantly higher than that of the Pt/CeO₂ catalyst because the addition of the proper amount of Au to the Pt/CeO₂ catalyst created a favorable density of state for the RWGS reaction. However, a higher density of state leads to a greater electron donation from the Au-doped Pt/CeO₂ catalyst to an antibonding orbital of CO₂, which weakens the O–C–O bonds and accelerates the methanation reaction. It

is hypothesized that by managing the density of the state close to the Fermi level, the Pt/CeO₂ catalyst's increased CO selectivity could be realized.

RWGS reactivity is enhanced in real reactions by the dual effect of Pd₁–FeO_x single-atom catalysts (SACs), as Du et al. reported [66]. Unexpectedly, Pd SAs not only offer single active sites but also dynamically carburize the FeO_x surface over an extended reaction period. This results in exceptional RWGS activity (42.0 mmol CO·g_{cat}⁻¹·h⁻¹) and CO selectivity (>98%), surpassing the results of other documented Fe-based catalysts. The results of this dynamic carburization show that the atmospheric rWGS reaction produces a highly active Fe₅C₂ phase with the lowest activation barrier of 27.7 kJ/mol. These results are obtained using cutting-edge characterization techniques. Compared to Pd nanoparticles with a fast FeO_x encapsulation that prevents carburization, SACs' dual effect produces better catalytic performance. The various functions that individual atoms play in actual reactions are revealed by this work, suggesting that SACs have a broader function. During actual reactions, single atoms play a dual role in the formation of a highly active phase of heterogeneous catalysts in addition to serving as independent active sites. It is important for rational designs to take into account both roles.

A series of monodispersed Pd nanoparticles, ranging in size from 2.8 nm to 8.1 nm, were prepared by Yang et al. [67] in a progressive manner. With regard to Pd sizes, the photo-thermal catalytic activity in the RWGS reaction exhibits a volcano-type dependence, with the highest activity occurring at a Pd/TiO₂ size of 6.3 nm. The tunable-surface electronic properties, such as the quantum size effect and metal-support interaction, are responsible for the size-modulated activity.

2.3.3. Ru-Based Catalysts

Some researchers have also turned their attention to the research of Ru-based catalysts [45,46,72–75], which we briefly describe below.

Tang et al. [72] prepared an efficient RWGS catalyst by encapsulating a Ru cluster with a size of 1 nm in a hollow silica shell. The space-confined structure prevents the sintering of Ru clusters, and the permeable silica layer allows the diffusion of gaseous reactants and products. This catalyst with reduced particle sizes not only maintains the excellent activity of Ru in the CO₂ hydrogenation reaction but also exhibits close to 100% CO selectivity and excellent stability at 200–500 °C.

Abdel-Mageed et al. [45] investigated the effect of carrier particle size on the performance of highly active Ru/TiO₂ catalysts and found that after high-temperature reduction treatment, the selectivity of TiO₂ particle size can be controlled from 100% methanation to 100% CO. The comprehensive characterization of the catalysts shows that while the reaction behavior changes, their structure, chemical, and electronic properties also change significantly. The chemical modification of the carrier via oxygen-vacancy formation leads to the electronic modification of the Ru centers around the interface, which in turn affects the reaction behavior of these centers in CO₂ reduction reactions, from methanation to RWGS reactions.

Wu et al. [73] reported effective photocatalysis driven by sunlight over Ru clusters supported by MXene that have strong light-absorption capabilities, high sintering resistance, and increased metal loading. Remarkably, MXene-supported Ru clusters demonstrated superior photothermal catalytic performance compared to silica-supported Ru clusters and MXene-supported Ru nanoparticles by 2 and 81 times, respectively. The superior photothermal characteristics of MXene materials and the robust binding between metal clusters and MXene supports are the cornerstones of our approach. Remarkably, the CO production rate of Ru clusters supported by MXene in the batch reactor was 4.0 mol·g_{Ru}⁻¹·h⁻¹, one of the highest recorded rates for photothermal RWGS catalysts to date. This approach can, in theory, be expanded to metal catalysts with even greater dispersion to promote the development of effective sunlight-driven single-atom catalysis. Future research will thoroughly examine how light affects catalytic reactions, with the goal of adding more photochemical activation to increase photocatalytic efficiency. Their work shows the great potential of

metal cluster catalysis powered only by concentrated solar radiation. Developing catalysts with enhanced reactivity and solar power alone presents excellent potential as a low-carbon chemical technology.

Chen et al. [74] examined the mechanisms of the RWGS reaction on Ru adsorption on a three-fold site of the CeO₂(111) surface using first-principles calculations and microkinetic simulations. Microkinetic simulations covering all elementary reaction steps were used to investigate the effects of temperature on the active site and the preferred reaction mechanism. Ru(OH)₃–(OH) is the predominant active site at low temperatures, according to the microkinetic simulations. A low barrier to direct CO dissociation is the outcome of this hydroxyl-promoted configuration. RuO₃ becomes the predominant active site when the temperature rises due to decreased Ru(OH)₃–(OH) abundance. The Mars–van Krevelen mechanism is the one that is favored in such circumstances. Heat makes forming oxygen vacancies easier, which serve as CO₂ anchoring sites. When CO₂ adsorbs, the oxygen vacancies are restored, increasing the CO₂ molecule's reactivity and facilitating the simultaneous scission of C–O bonds and CO desorption. Ultimately, their research suggests a temperature-dependent RWGS mechanism and emphasizes the impact of surface hydroxyl and oxygen vacancies on RWGS compared to the Ru/CeO₂ single-atom catalyst.

2.3.4. Au–Based Catalysts

In addition to the above precious metal catalysts, some Au-based catalysts have also been studied and reported, and the following is a brief introduction.

Abdallah et al. [34] loaded a titanium dioxide and zirconia support with a very low content (<0.1 wt%) of Au, used it for the RWGS reaction, and found that this gold-based catalyst showed high catalytic activity for the RWGS reaction at low temperatures. At 250 °C, the catalytic activity of the Au/TiO₂ catalyst is nearly 10 times that of Au/ZrO₂. The in situ infrared DRIFT results show that the formate is the main intermediate species on the Au/ZrO₂ catalyst, while on the Au/TiO₂ catalyst, the reaction is carried out via the formation of hydroxyl carbonyl intermediates. The results of scanning transmission electron microscopy (STEM), STEM–EELS (electron–energy–loss spectrometry), XPS, and EPR in situ indicate that the Au–O_v–Ti³⁺ interface sites are responsible for the excellent activity of Au/TiO₂.

To bridge the knowledge gap regarding the completeness of the plasma–thermal coupling mechanism for Au/γ–Al₂O₃, Wang et al. [76] studied the photo–thermocoupled catalytic RWGS reactions and their reaction pathway and plasmonic enhancement mechanism. As per the findings, the total reaction is facilitated by both the formate and carboxyl pathways. A low reaction temperature over small Au NPs is proposed to be mediated primarily by the m–formate pathway. Combining resonance and hot-electron energy-transfer mechanisms, spectro–kinetics, and theoretical computation analyses show that the plasmonic energy preferentially moves to HCOO*. As the rate–determining step (RDS) of the entire RWGS reaction, the plasmonic energy facilitates the dehydration of HCOO* to CO.

2.3.5. Some Other Precious Metal-Based Catalysts

In addition to introducing the above precious metal catalysts, here we also introduce these relatively less reported precious metal catalysts, such as Bi, Pt–Re, Re, Rh, Ir, In, etc.

Kang et al. [77] reported a Bi-based photothermal RWGS catalyst. Using a soft template technique, they were able to create Bi single atoms loaded with CeO₂ nanosheets that demonstrated exceptional stability and activity for RWGS at 400 °C air corrosion, demonstrating previously unheard-of oxidation resistance. High activity and oxidation resistance for RWGS result from the Bi single atoms' low energy barrier and their +3 valence state retention during RWGS, as demonstrated via experiments and first-principles calculations. Loading BiO_x/CeO₂ into a Ti₂O₃–based photothermal system resulted in a CO generation rate of 31.00 mmol g^{−1} h^{−1}, four times higher than the state–of–the–art

for solar-driven RWGS under 20 sun irradiation units. This was accomplished under three sun units of radiation.

RWGS reaction tests were conducted by Liu [43] on Pt–Re/SiO₂ catalysts that varied in Re content and were prepared via co-impregnation. The results of the characterization showed that the oxophilic ReO_x ($0 \leq x \leq 3.5$) that was close to the Pt particle changed the surface of Pt by partial coverage and electronic interaction, which led to a decrease in the number of sites and a weakening of the strength of CO adsorption. When Pt/Re/SiO₂ is optimized (Pt/Re = 1.91), the turnover frequency (2.30 s^{-1}) is 3.9 times higher at 400 °C than when Pt/SiO₂ is used under differential conditions, and the apparent activation energy is decreased. Pt–Re/SiO₂'s CO selectivity maintained >96.2% under integral conditions, unlike Re/SiO₂, which generated a significant amount of CH₄. Pt helps to activate H₂, while ReO_x, an oxophile, helps to activate and adsorb CO₂. This was determined using reaction order analysis. The RWGS activity is enhanced while CH₄ production is inhibited by the perimeter sites at the Pt/ReO_x interface that have balanced hydrogenation and C–O cleavage properties.

Yang et al. [78] clearly demonstrated the close relationship between the size effect, the active site, and the reaction mechanism using a special set of well-defined TiO₂-supported Re catalysts and systematic characterizations. Additionally, a size-dependent, wave-like activity of CO₂ conversion was found. CO₂ hydrogenation is regulated by the RWGS reaction in the size range of a single atom to 1.0 nm. As size increases, the turnover frequency of this reaction falls. Nevertheless, CO₂ methanation takes over as the primary reaction and exhibits a size-dependent performance resembling a volcano for clusters larger than 1 point 0 nm. According to the mechanistic analysis, formate pathways in single-atom catalysts allow the perimeter site to control the RWGS reaction. The edge site in the Re cluster, on the other hand, serves as the active site. Here, CO₂ undergoes a redox process to reduce CO and then hydrogenates to methane across the edge sites. This finding could contribute to a better mechanistic understanding of structure sensitivity.

In Liu's work [79], it was successfully constructed to perform the reverse water–gas shift reaction mediated by the diatomic anion Rh^{2−}. At room temperature, the production of a gas–phase H₂O molecule and the ion product [Rh₂(CO)_{ads}][−] were clearly identified, and the desorption of CO from [Rh₂(CO)_{ads}][−] was the only basic step that needed additional energy to finish the catalysis. Since designing efficient routes to yield H₂O from CO₂ and H₂ is difficult, this experimentally identified Rh^{2−} anion represents the first gas–phase species that can drive the RWGS reaction. Their recently created double-ion trap reactors were used to carry out the reactions, which were then examined using high–precision quantum-chemical calculations, photoelectron spectroscopy, and mass spectrometry. They discovered that the distribution of the final products (D₂O and Rh₂CO[−]) and the reactivity were not significantly affected by the order in which the reactants (CO₂ or D₂) were fed into the reactor. The essential steps to steer the reaction in the direction of the RWGS were revealed with atomic precision.

In Lu's work [80], a solvent evaporation self-assembly method was used to build a system of Ir species and α–MoC. Because of the synergistic effect of Ir and α–MoC, the catalytic performance of the Ir/MoC catalysts for the RWGS reaction was significantly better than that of pure α–MoC over a wide temperature range (200–500 °C). At 500 °C, 0.1 MPa, and 300,000 mL·g^{−1}·h^{−1}, the ideal 0.5% Ir/MoC catalyst produced a 48.4% CO₂ conversion, similar to the equilibrium conversion of 49.9%. Higher than most previously reported values, the CO selectivity and space–time yield of CO over 0.5%Ir/MoC reached 94.0% and 423.1 umol·g^{−1}·s^{−1}, respectively. Furthermore, over a 100 h period, 0.5% Ir/MoC maintained its catalytic properties and showed exceptional stability at elevated temperatures. It was shown via several characterization techniques that the Ir species supported on α–MoC substrates were widely distributed. The stability of the Ir/MoC catalysts was significantly enhanced by the strong metal–support interaction that took place via electron transfer between Ir and α–MoC. Ir single atoms (Ir₁) and clusters (Ir_n) coexisted to form Ir_n–Ir₁–C–Mo synergistic sites between Ir and α–MoC for the Ir/MoC catalysts with

Ir loadings > 0.2% (mass fraction). Comparing the 0.5% Ir/MoC catalyst to the other Ir/MoC catalyst, the number of Ir₁ species and size of Ir_n species were higher and smaller, respectively. The exceptional adsorption and activation of CO₂ and H₂ during the RWGS were facilitated by the optimal electron density conferred upon 0.5% Ir/MoC. The RWGS reaction mechanism was found to occur via a formate pathway in in situ diffuse-reflectance infrared Fourier transform spectroscopy experiments. The creation and breakdown of formate intermediates were noticeably aided, even though the Ir_n–Ir₁–C–Mo synergistic site formation had no effect on the reaction mechanism. The synergistic effect, therefore, effectively increased the catalytic performance of Ir/MoC. This work offers guidelines for creating stable and effective CO₂ utilization catalysts.

With In₂O₃, Mhamane's work [81] showed a sustainable catalytic CO₂ conversion to almost 100% CO selectivity at room pressure. Using less hydrogen in the feed than stoichiometric amounts, it is important to note that high CO yield may be observed at the expense of unwanted methanation; 1:1 and 1:0.67 CO₂:H₂ ratios show 98–99.6% CO selectivity with 25–38% CO₂ conversion between 773 and 873 K. For the reverse water–gas shift reaction, an ideal reactant composition is present when CO₂ and H₂ conversion occurs under steady-state conditions at 773–873 K, suggesting a 1:1 ratio of adsorbed reactants (with 1:0.67 CO₂:H₂ feed) on the catalyst surface. In contrast, H₂-rich feed compositions indicate the H₂-dominated surface. Using near-ambient pressure photoelectron spectroscopy (NAPPES) to investigate surface electronic structure changes under near-operating conditions, the following intriguing results were found: (a) Higher temperatures caused a shift in the valence band to lower binding energy, up to 0.6 eV. (b) Active oxygen vacancy site formation modifies the In₂O₃ work function and is responsible for the catalyst surface's observed heterogeneous nature under NAPPES measurement conditions. (c) It is discovered that the aforementioned alterations are reversible upon cessation of the reaction. We found that in the active temperature window of the catalyst supporting the heterogeneous reaction, the vibrational characteristics of the reactant molecules were widened.

Precious metal catalysts (Pt, Pd, Au, Rh, Ru, Ir, etc.) are not easy to deactivate, although they have high catalytic activity and stability. However, due to their high prices and scarce resources, they are limited in large-scale applications in industrialization and are only suitable for laboratory mechanism research. Therefore, efforts are needed to find some alternative catalysts to precious metals.

2.4. Non-Precious Metal Catalysts

Although precious metal catalysts have excellent CO₂ reduction performance and stability, their high cost limits their large-scale industrial application. Therefore, the exploration of inorganic non-precious metal catalysts has attracted widespread attention from scientific research staff, and non-precious metal catalysts (Cu, Ni, Fe, Mo, etc.) are often used to replace precious metals because of their low cost and good catalytic activity.

2.4.1. Ni-Based Catalysts

Nickel-based catalysts experience the problems of easy sintering and carbon deposition in the RWGS reaction and have low selectivity for CO. Several examples of design, preparation, and mechanism research on nickel-based catalysts are listed below.

Zhang et al. [48] prepared a sulfur-containing Ni/ZrO₂ catalyst to improve CO₂ conversion and regulate CO₂ hydrogenation selectivity. The effect of carrier size on the catalytic performance of RWGS was investigated. The results show that the 80 nm Ni/ZrO₂ sample with a smaller carrier size had higher Ni dispersion and oxygen-vacancy concentration, had more exposed active centers, and displayed improved adsorption and activation ability of CO₂.

Gong et al. [82] proved that the interfacial synergism of Ni/Ga₂O₃ promoted the selective hydrogenation of CO₂ to CO (CO selectivity > 95%) in the temperature range of 350–450 °C. Studies show that the synergistic effect of the Ni/Ga₂O₃ interface significantly affects the adsorption of H₂ and CO₂, resulting in the formation of different intermediates

and products. *HCOO preferentially forms on the Ni surface and is further hydrogenated to CH_4 and H_2O . In contrast, the Ni/ Ga_2O_3 interface favors the formation of CO with the help of H_2 . This study provides a highly selective catalyst for the RWGS reaction in the CO_2 hydrogenation process and promotes the surface modification of the catalyst to improve the activity and selectivity.

Our group [8] prepared NiCe–HMS and Ni–HMS limited-structure catalysts using the one-pot method and conducted RWGS tests in the 500–750 °C temperature range. Compared with Ni/HMS catalysts prepared via the traditional impregnation method, Ni–HMS and NiCe–HMS showed higher CO selectivity. This is due to the formation of highly dispersed nickel nanoparticles on the surface of the carrier, which inhibits the formation of CH_4 .

Zhang et al. [83] reported the activity and selectivity of Ni-rich nickel phosphide catalysts for CO_2 hydrogenation for the first time. Their findings demonstrate that Ni_2P/SiO_2 is an extremely effective catalyst for RWGS, yielding more than 80% of CO throughout the entire 350–750 °C temperature range.

Shen et al. [84] discovered that Ni doping (1.0–Ni– CeO) significantly increased the RWGS reaction activity of pure CeO_2 at low temperatures. At 300 °C and a WHSV of $60,000 mL \cdot g^{-1} \cdot h^{-1}$, the Ni–based mass–specific CO formation rate of 1.0–Ni– CeO_2 could reach up to $1542 mmol \cdot g_{Ni}^{-1} \cdot h^{-1}$. Furthermore, it was established through our experiments and density functional theory calculations that the surface defects serve as the active sites for H_2 heterolytic dissociation, which is the RWGS reaction's rate-determining step. In 1.0–Ni– CeO_2 , the formed Ce–H species is stable. Furthermore, the superior H_2 heterolytic dissociation capacity and high active H^- released from the Ce–H species of 1.0–Ni– CeO_2 at low temperatures are responsible for its increased catalytic activity and selectivity. Moreover, CO–TPD (temperature–programmed desorption) and CO DRIFTS demonstrated that 1.0–Ni– CeO 's 100% CO selectivity was primarily due to its lower CO affinity. A new reaction mechanism was revealed using systematic in situ DRIFTS analysis. According to this mechanism, CO_2 was first adsorbed on the hydroxyl groups of $Ce^{3+}-OH$ rather than on oxygen vacancies, which resulted in the formation of the bicarbonate intermediate (*HCO_3). The bicarbonate intermediate was then reduced to formate (*HCOO), and the highly active H^- in Ce–H caused the production of CO. This work may open up new avenues for the development of robust, affordable, and efficient catalysts for hydrogenation reactions at low temperatures.

In addition, many other nickel catalysts have been reported [48,49,85–98], including bimetallic [93–98] or polymetallic catalysts composed of nickel and other metals.

2.4.2. Fe–Based Catalysts

Fe–based catalysts [50,99–105], as typical high-temperature catalysts, have also been used in RWGS reaction studies. Here are some selected examples. The carrier–free nano ferric oxide catalyst prepared by Kim et al. has high catalytic activity and stability [50]. Through transmission electron microscope observation, it was found that nano iron oxide did not easily agglomerate during the RWGS reaction. XPS and X–ray diffraction (XRD) show that atomic carbon and oxygen formed due to dissociative chemisorption of CO or CO_2 appear to diffuse into many nanoparticles to form Fe oxides and Fe carbides. C and O are produced by the reactants on the surface of the iron oxide, and CO_2 and CO are diffused into the body of the iron oxide nanocatalyst. Therefore, during the RWGS reaction, the structure of the catalytically active surface consisting of metal Fe remains unchanged, so the catalytic activity remains stable for a long time. For Fe–based catalysts, it is still a subject of debate as to whether the active phase is metallic iron, iron oxide, or iron carbide.

Bogdan et al. [99] investigated, for the first time, the reduction of CO_2 to CO with hydrogen on alumina–supported Co and Fe catalysts under supercritical conditions with CO or CH_4 as the target product. The selectivity of the Co/ Al_2O_3 catalyst for methanation is close to 100%, while the Fe/ Al_2O_3 system shows an advantage for hydrogenating CO_2 to CO and significantly forms ethane (up to 15%). Compared with the gas–phase

reaction, the spatio-temporal yield can be increased by one order of magnitude under supercritical conditions. The difference in the crystal phase characteristics of the iron-containing catalyst leads to the reverse water-gas transfer reaction to produce carbon monoxide, while the reduced iron phase leads to the Fischer-Tropsch reaction to produce a mixture of hydrocarbons. Direct methanation occurs selectively on Co catalysts. Methanol formation was not observed on the studied Fe and Co catalysts.

Zhang et al. [100] found that metallic iron was a better RWGS catalyst than Fe₃C. The addition of Cs and Cu can promote the activity of Fe⁰, hindering the carburization of iron while favoring higher conversion rates and selectivity. When stability tests were performed, the catalyst aged during the RWGS reaction, and a new phase appeared: Fe₅C₂ (Hagg carbide). For RWGS reactions, Fe₅C₂ is an excellent catalyst with a higher carbon dioxide conversion rate than samples in which Fe⁰ is the active phase. However, Fe₅C₂ has a low CO selectivity compared to Fe⁰-based samples. The results showed that the best activity/selectivity was achieved by fine-tuning the Fe/Fe₅C₂ ratio.

Watanabe et al. [101] used H₂S as a co-feeding gas to investigate the catalytic activity of Fe/CeO₂ on the RWGS reaction and maintained a stable activity for 12 h. In addition, co-feed H₂S can be used as a hydrogen source for RWGS.

In Xu's study [102], the comparison of dynamic and steady-state CO/CO₂ hydrogenation performance showed a large amount of FeO_x covering the χ -Fe₅C₂-dominated bulk phase during CO₂ hydrogenation. The overall RWGS rate was positively correlated with the surface content of FeO_x under differential conditions (CO₂ conversion < 10%) and negatively correlated with the surface content of FeO_x under integral conditions (CO₂ conversion > 10%).

Their findings help us to understand the role of different types and amounts of iron sites on Fe-based catalysts during CO₂ hydrogenation. Adjusting the number and properties of different surface sites to achieve optimal intersite synergies may stimulate the development of future multi-site CO₂ hydrogenation catalysts.

2.4.3. Cu-Based Catalysts

Cu-based catalysts have attracted much attention because of their low price, high activity at relatively low temperatures, and good selectivity to CO. However, since copper is easily sintered or coked, such catalysts are prone to deactivation during the RWGS reaction. In order to overcome these shortcomings, many RWGS reactions catalyzed by Cu-based catalysts have been reported [39,51–53,106–131], and we will describe some representative examples in detail.

Ai et al. [106] discovered that the grinding process could enhance the amount and distribution of Cu⁰ species on the surface and that the Cu content could control the amount and distribution of Cu⁰ species' crystallinity. Moreover, the low crystallinity of Cu⁰ species could encourage the exposure of CO₂-hydrogenation active sites.

Zhuang et al. [51] added Ru to the Cu/ZnO/Al₂O₃ catalyst for the RWGS reaction. The CO₂ conversion rate was more than two times higher than that of the Cu/ZnO/Al₂O₃ catalyst. At the same time, the stability of the catalyst was significantly improved. Through XRD, scanning electron microscope-energy-dispersive spectroscopy (SEM-EDS), scanning transmission electron microscope-energy-dispersive spectroscopy (STEM-EDS), and TPR characterization, it was found that this may be due to the formation of Ru-Cu core-shell nanoparticles. In addition, the interaction between Ru and the support is also an important factor affecting catalyst selectivity.

Liu et al. [38] constructed stable copper clusters in a Cu/CeO₂ catalyst with a high copper loading capacity of 15 wt%. Under very harsh reaction conditions, CeO₂ nanorods were partially sintered, forming 2D and 3D copper clusters on their surfaces. This partially sintered catalyst exhibits unparalleled activity and excellent durability at high temperatures. The interaction between copper and CeO₂ ensures that the copper clusters are stably anchored to the CeO₂ surface. The large number of in situ surface-oxygen vacancies causes a synergistic effect with adjacent copper clusters, which promotes the reaction.

Deng et al. [39] prepared catalysts with different copper loads using the simple impregnation method via NaOH-activated slag-polymer microspheres (SGSs) as the carriers. The results show that the 10% Cu/SGS catalyst has better CO₂ conversion performance. At 550 °C, the CO₂ conversion and CO selectivity of the 10% Cu/SGS catalyst reached 48% and 96%, respectively. The results show that the high performance of the catalyst is mainly due to the interaction between copper and the SGS carriers and the adsorption and activation of CO₂ by the alkaline center on the SGS carriers.

Liu et al. [107] loaded Cu onto titanium dioxide nanotubes (TiNT) and titanium dioxide nanoparticles (TiNP), and the RWGS activities of the two catalysts were different. The activity of the nanoparticle carrier is very low, and the content of Cu hardly changes the activity, but the activity of the nanotube carrier is very high and has three different behaviors as the surface density of copper increases. At a low surface density, an active Cu–O–Ti site with low apparent activation energy is formed. At a higher surface density, copper nanoparticles are formed on the surface of TiNT, and the reaction barrier is reduced. At moderate surface densities, the metal copper clusters are engulfed by a TiO_x overlay formed during hydrogen treatment, similar to the overlay formed by classical strong metal carrier interactions (SMSI). These reducing layers are significantly more active against RWGS than the initial TiNT surface but have similar activation barriers, higher than those on exposed copper and TiNP surfaces. SMSI is an important concept in heterogeneous catalysis, but it will inevitably sacrifice catalytic activity due to over-coverage.

González-Arias et al. [108] prepared a series of Cu–MnO_x catalysts and found that the improvement in catalyst performance was due to the addition of Mn to enhance the dispersion of Cu and increase the surface alkali concentration. Under standard RWGS conditions, the highest reaction rate of the catalyst is related to the improvement of Cu dispersion and the composition of the highly active Cu–MnO_x domains. It is worth noting that the change in the optimal copper–manganese ratio is a function of the RWGS reaction conditions.

Ebrahimi et al. [52] prepared a Cu/CeO₂ solid solution using the combustion synthesis method. The produced catalyst exhibited high activity, stability, and 100% CO selectivity in the RWGS reaction, and these catalytic activities were attributed to the excess oxygen vacancy on the CeO₂ surface, which could promote CO₂ conversion. The high activity of this catalyst is due to the synergistic effect between the active Cu⁰ and Ce³⁺–oxygen vacancy.

Yang et al. [109] reported the reduction reaction of carbon dioxide catalyzed by Cu–CeO₂ under visible light and speculated regarding a reaction mechanism induced by the localized surface plasmon resonance effect with the assistance of visible light. The specific reaction process is divided into four steps [Figure 4]: (I) hot electrons and hot holes are produced via the plasmon effect of Cu when visible light is present; (II) hydrogen dissociation and spillover are accelerated via the hot holes' reaction with hydrogen; (III) CO is produced via the hot electrons attacking and transferring to the intermediate species; and (IV) vibrant light exposure causes the oxygen vacancies to regenerate.

Zhang et al. [53] studied a variety of strategies to effectively regulate nanointerfaces from different aspects, such as carrier composition, Cu preparation parameters, and pre-treatment and reaction conditions, in order to balance the activity and stability of Cu/TiO₂ catalysts in RWGS reactions. The results show that due to the reducibility of TiO₂ and the limited electron transfer from TiO₂ to Cu, only doping Zn in the TiO₂ carrier can inhibit the formation of nanointerfaces during the reduction treatment. Cu coverage on Zn-modified TiO₂ is significantly decreased, but the catalytic activity is increased by 44%, and the stability is unchanged.

In addition to the specific examples mentioned above, many other researchers have reported interesting works [39,53,110–131] on copper catalysts, mainly focusing on catalyst design and mechanism studies.

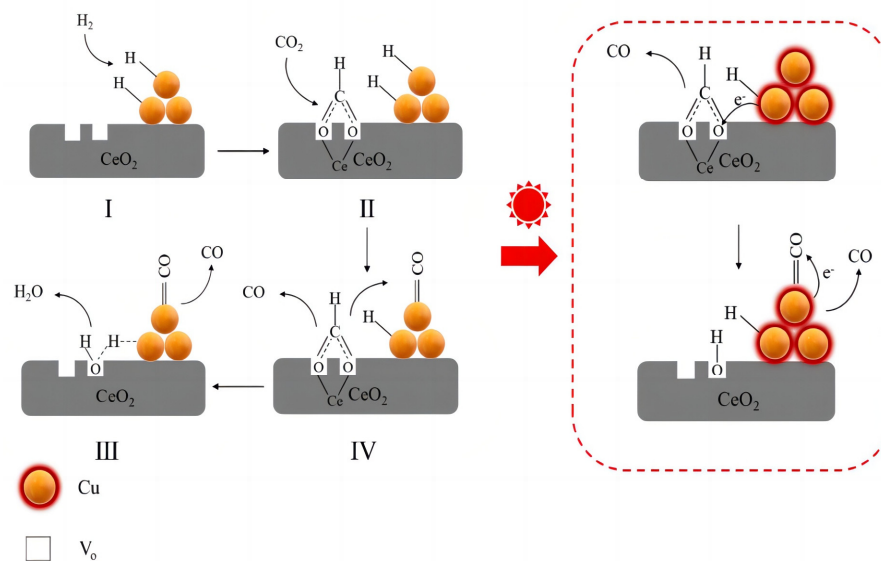


Figure 4. The proposed mechanism of the RWGS reaction under visible–light irradiation.

2.4.4. Mo-Based Catalysts

Molybdenum is more abundant and cheaper than precious metals, increasing the potential for large-scale industrial applications of molybdenum-based catalysts. Molybdenum-containing catalysts are widely used, including Ni–Mo catalysts [132], molybdenum sulfide catalysts [133], MoO_x catalysts [54], supported Mo-based catalysts [55,134], new Mo_2C and Mo_2N catalysts [135], etc. A few representative examples are described below.

Xin et al. [136] found that during the CO_2 hydrogenation reaction, Ru– MoO_3 formed a strong metal–support interaction (SMSI) state between the metal and the carrier at 250°C , which was conducive to CO_2 selective hydrogenation to form CO. During the reaction, Ru nanoparticles promote the reduction of MoO_3 to form an active MoO_{3-x} coating with oxygen vacancies, which migrates to the surface of Ru nanoparticles to form a coating structure (Ru@ MoO_{3-x}). The resulting SMSI state changes the catalytic performance of the catalyst from 100% methanation at the Ru site on the exposed surface to 99% CO formation via the quasi-MvK (Mars–van Krevelen) mechanism in the MoO_{3-x} layer. Selective regulation is achieved through different SMSI states in the CO_2 hydrogenation reaction.

Ronda [56] et al. took advantage of the high thermal stability and excellent electrical conductivity of the MAX phase to prepare a $\text{MoO}_3/\text{Ti}_3\text{AlC}_2$ catalyst to increase its intrinsic RWGS activity. When molybdenum oxide is loaded on the MAX phase of the Ti_3AlC_2 , the low surface area of the MAX phase leads to the formation of large MoO_3 rods with blocky characteristics. The presence of electron-rich Ti_3AlC_2 enhanced the redox characteristics of MoO_3 in the RWGS reaction, resulting in a high degree of surface reduction and the formation of many oxygen vacancies. Therefore, the catalyst showed the highest activity in catalytic experiments. When the MAX phase acts as a carrier, the electron-rich Mo site is an ideal activation site for CO_2 via electron transfer to the CO_2 antibond orbital, an interaction that weakens the C–O bond and favors reduction to CO. The catalyst is selective to CO, thus inhibiting the formation of methane and coke.

Zhang et al. [54] found that the surface modification of Ni by MoO_x can regulate RWGS and methanation reactions. The addition of MoO_x improves the dispersion of Ni through strong interaction, and the partially reduced MoO_x modifies the surface of Ni particles using covering and electron modification, which enhances the desorption of CO on the surface. The addition of a large amount of Mo (Mo/Ni ratio of 1) causes the reaction to shift to RWGS and the CO selectivity to be greater than 94%. Kharaji et al. [57] incorporated Mo into the $\text{Fe}/\text{Al}_2\text{O}_3$ catalyst and found that Mo greatly improved the RWGS catalytic activity and CO selectivity due to the Fe–O–Mo structure formed in the $\text{Fe}_2(\text{MoO}_4)_3$ phase

of the Fe–Mo/Al₂O₃ catalyst. The presence of the Fe–O–Mo structure causes Fe₂(MoO₄)₃ to have a lower reducibility, which effectively inhibits the reduction in Fe oxides. On the other hand, the existence of the Fe–O–Mo structure promotes the flow of electrons from Fe to Mo, resulting in the Fe species being in an electron-deficient state and forming a positive surface charge, which is detrimental to the adsorption of CO and effectively inhibiting the further hydrogenation of CO. As an additive and active component, Mo shows good CO selectivity, but its CO₂ conversion needs to be improved.

Zhang et al. [137] reported the preparation of Cu–Cs–MO₂C using Cu as an accelerator and Cs as a dopant to improve the conversion and selectivity of the catalyst, respectively. It was found that the increase in CO₂ conversion was due to the addition of copper to provide more active sites for the catalyst, such as Cu⁺ and Cu⁰. Cs was due to its significant positive electric properties that create electron perturbations on the catalyst surface, thus enhancing catalytic performance. Its addition can improve CO selectivity, especially at low temperatures. In addition, the carbon-doped catalyst appears to be activated in situ due to the recarburizing phenomenon, which results in the catalyst being fairly stable in continuous operation.

Zhang et al. [138] used silica as the carrier to prepare a Mo–P–SiO₂ catalyst and found that the catalyst was completely oxidized through characterization. It was found that the high selectivity of carbon monoxide was due to the MoP phase generated on the surface of the silica carrier, which was more conducive to the direct conversion of carbon dioxide into carbon monoxide through MoP(0001). Based on the potential energy–surface profile, methane generation on the MoP(0001) surface requires higher energy than carbon monoxide. In other words, the MoP(0001) surface is more selective for producing CO than CH₄.

Yuan et al. [139] reported the application of Ni-doped MoS₂ in CO₂ hydrogenation into methanol and prepared a series of MoS₂/Ni_x catalysts. Through DFT calculations, they found that MoS₂/Ni-catalyzed CO₂ hydrogenation follows the oxidation–reduction pathway, and the optimal adsorption structures and barrier energies of different intermediates were shown in the article. CO₂ and H₂ are directly dissociated from CO*, O*, and 2H* by an energy barrier of 0.63 eV. The large adsorption energy indicates that CO* has a strong interaction with MoS₂ (E_{ads} = −1.27 eV) and is more likely to react further on the carrier without releasing CO.

2.5. Other Catalytic Systems

2.5.1. Transition Metal Carbide Catalysts

Transition metal carbide catalysts (TMCs) are also promising and attractive catalysts; after the introduction of carbon, the electronic properties of these catalysts change, meaning that their activity becomes similar to that of precious metal catalysts, with a strong H₂ dissociation and CO bond-breaking ability, and showing high activity in the CO₂ hydrogenation to CO reaction. Therefore, it has been reported that catalysts such as vanadium carbide [140], tungsten carbide [141,142], cobalt carbide [143], and molybdenum carbide [126,144–149] have superior catalytic activity and CO selectivity when applied to RWGS reactions.

Juneau et al. reported K-promoted tungsten carbide with porous γ -Al₂O₃ as the carrier for RWGS in 2019 [141]. Later, they [142] found that micellar-based silica coating technology could prepare a 10 nm tungsten carbide nanoparticle catalyst. The high activity and CO selectivity of nano-WXC carburizing observed at 1000 °C may be due to the fact that the coated silica maintains a particle size of 10 nm during carburizing, thus promoting the formation of surface carbides. Compared with the catalyst prepared via the impregnation method, the synthesis method affects the formation degree of W × C and the reactivity of RWGS. In Zhang's [143] paper, they described a mechanism for controlling the formation and quantity of carboxylate species on hollow cubic Co₃O₄ (without Mn), thereby modifying the surface energy and crystal growth rate. At 270 °C, where CO₂ conversion was almost at its thermodynamic limits at a space velocity of 60,000 mL g_{cat}^{−1} h^{−1}, Co₂C nanoprisms demonstrated excellent activity in RWGS. Reaction mechanisms and kinetics

studies were used to correlate the catalytic performance of Co_2C nanoprisms with highly active surfaces (020) and (101), as well as double reaction pathways (redox and formate routes). This work shows great potential for bridging RWGS and sequential cascade reactions, and it offers a way to design and modulate the morphologies of transition metal carbides. Reddy [144] synthesized Mo_2C using the direct carbonization of Mo precursors. Under 723 K and 1 atmospheric pressure with a molar ratio of $\text{CO}_2/\text{H}_2 = 1:3$, the conversion of CO_2 catalyzed by Mo_2C can reach 57%, and the CO selectivity can reach 62%. Marquart et al. [145] prepared four catalysts using three different synthesis processes with good catalytic activity. The results show that CO_2 forms adsorbed oxygen surface species by dissociating on the carbide surface. Above 850 K, the carbides oxidize into the oxide phase MoO_2 or MoO_3 . The different catalysts all exhibit CO_2 conversion rates higher than 30%, and the CO selectivity is 99% even at high H_2/CO_2 ratios. Although the new molybdenum carbide catalyst has excellent activity in the RWGS reaction, its preparation method is difficult compared with other catalysts.

2.5.2. Perovskite-Type Catalysts

Mixed metal oxides with ABO_3 -type perovskite structures acting as carriers of rare earth metals and transition metals are considered to be very promising catalytic ceramic materials [150]. The catalytic properties of perovskites can be modulated by changing the properties of A and B ions or inserting dopants into the structure. Perovskite oxides have attracted the attention of researchers due to their high mobility of oxygen and ability to stabilize unusual cationic oxidation states, as well as their thermal stability at high temperatures [151]. Alkali metals, alkaline earth metals, and rare earth metals are commonly used as accelerators, which can change the acid–base properties of the catalyst, improve the dispersion of the active species, and increase the strength of the interaction between the active species and the carrier. Kim et al. [152] added Y, Zn, and Ce to BaZrO_3 and discussed the influence of dopants on the catalytic activity. At 600 °C for 5 h, all catalysts showed stable catalytic properties. Among them, the $\text{BaZr}_{0.8}\text{Y}_{0.16}\text{Zn}_{0.04}\text{O}_3$ (BZYZ) catalyst showed excellent activity with a CO_2 conversion rate of 37.5% and CO selectivity of 97%. Ce insertion improved the ionic conductivity of BZYZ, but additional Ce did not have any positive effect on the catalytic activity of the RWGS reaction. Jo et al. [153] examined the effects of controlled template removal and nanocasting on $\text{La}_{0.8}\text{Sr}_{0.2}\text{FeO}_3$ (LSF). The nano–cast LSF has a mesoporous structure due to using the SBA–15 template, and further etching enhances its textural characteristics. Characterization verified the high dispersion of metal–active sites on nano–cast LSF. RWGS operating at 600 °C used LSF as oxygen carriers with varying silica contents. It was discovered that the CO yield rose as the silica residue in LSF decreased; however, the catalyst’s mesoporous structure would be destroyed by excessive etching, removing too much silica (<5 wt%). An LSF with a 10 wt% silicon content outperforms RWGS. The surface–oxygen–to–lattice–oxygen atomic ratio could be a crucial factor in determining the reaction’s reactivity. The photothermal catalyst Ni/LaInO_3 designed by Yu et al. [154] can convert CO_2 into nearly uniform CO in a H_2 –rich environment with a high generation rate, which promotes the adsorption and activation of CO_2 . Due to the photoelectric effect, the RWGS reaction time can be significantly reduced. This study provides a new idea for designing efficient photothermal catalysts to maximize the use of solar energy in the future and lays the foundations for regulating product selectivity during catalytic CO_2 hydrogenation.

In heterogeneous catalysis, the catalytic performance of bifunctional catalysts is often better than that of single-component catalysts. The shape, size, and distribution of catalytic particles also have a significant influence on the activity of the catalyst. Kopac et al. [155] theoretically studied the effects of bifunctional groups on RWGS reactions in detail. Density functional theory was used to calculate the energy diagram of RWGS on three surfaces (copper (111), SrTiO_3 surface, and Cu/SrTiO_3 interface between two solids). These three surfaces were combined using mesoscale dynamics Monte Carlo simulations to study the turnover and yield of CO production as a function of particle size. The results show that

the reaction speed at the interface is faster. However, in addition to the interface, the binding of copper and carrier sites further accelerates the RWGS reaction, suggesting that the catalyst's bifunction is manifested in more complex interactions between phases rather than just interface effects, such as hydrogen spillover. The authors found three different effects, namely an electronic effect, a synergistic effect, and a geometric effect, and a smaller Cu on the carrier SrTiO₃ showed a higher CO formation rate.

2.6. Catalyst Deactivation in the Reverse Water–Gas Conversion Reaction

Under high-temperature conditions, the catalyst used for RWGS reaction has poor thermal stability or weak interactions between the active component and the carrier, which leads to sintering and agglomeration of the catalyst at high temperatures and decreases the activity of the catalyst [58]. In addition, carbon deposition is also an important cause of catalyst deactivation. Carbon deposition, as the name suggests, means that the surface of the catalyst is covered by a certain form of carbon, and carbon is mainly formed via carbon-containing substances in the raw material breaking bonds on the surface of the catalyst or first coking and then dehydrogenation. These carbon species cover the active site, thus reducing catalyst activity. Therefore, the stability of the catalyst at high temperatures is extremely important for the RWGS reaction.

Yang et al. [58] mixed Fe into Ni/CeO₂–Al₂O₃, and the NiFe/CeO₂–Al₂O₃ catalyst showed an excellent CO₂ conversion rate in the stability test at 800,000 mL·g⁻¹·h⁻¹ and 700 °C. FeO_x greatly enhances Ni dispersion on the surface, which helps to provide higher activity in the reaction. In addition, the FeO_x–Ni interaction leads to electron enrichment of Ni surface atoms, and higher electron density is conducive to CO₂ adsorption. The 0.3CuMgAl–LDH–400 catalyst prepared using the hydrothermal method by Chen et al. [156] showed high stability during the RWGS reaction, and the activity remained unchanged for more than 30 h, which was due to the fact that the use of LDH as a carrier improved the dispersion of Cu and the presence of more alkaline sites. On the contrary, the catalytic activity of 0.3CuMgAl–IMP–400 prepared using impregnation decreased slightly after 20 h of the reaction. The results show that the catalyst prepared with LDH as the support has better stability.

Goguet et al. [59,157] studied the deactivation process of Pt/CeO₂ catalysts. The stability test results show that the initial CO₂ conversion rate is stable at 13.7%, and the CO selectivity is greater than 99%. As the reaction progresses, its catalytic activity begins to decrease gradually, possibly due to the catalyst's carbon deposition or the metal's sintering. In order to clarify the deactivation principle, the TPO cycle test was performed on the Pt/CeO₂ catalyst before and after the reaction. The results show a linear relationship between the degree of deactivation of the Pt/CeO₂ catalyst and the amount of carbon deposition. The place where carbon deposition occurs is the active part of the reaction. With the increase in time, the active part is gradually covered by carbon deposition, which leads to catalyst deactivation.

3. Conclusions

Converting carbon dioxide into high-value-added chemicals and fuels is a potential path to a carbon-neutral future. The reverse water–gas conversion reaction converts carbon dioxide into carbon monoxide and produces syngas, followed by methanation and the preparation of alcohols using Fischer–Tropsch synthesis, which is a promising method for carbon dioxide utilization. However, due to the endothermic reaction at low temperatures, the strong exothermic methanation reaction is competitive with the reverse water–gas change reaction. Although a high temperature is conducive to the forward reaction, the energy consumption of the reaction is too high. Therefore, developing catalysts capable of high conversion and selectivity at lower temperatures in the future will be a research focus for scientists. Transition metals ought to be the main subject of future research on the elemental makeup of active RWGS catalysts. Future resource shortages are inevitable, but they can be minimized by avoiding reliance on noble and rare elements. Targeting less

expensive components will also lower overall expenses. Common elements like Cu, Fe, and Mo are important for further RWGS research because they can significantly increase catalytic activity, particularly when combined with metal oxides as a support. Future theoretical and computational investigations, in addition to experimental catalytic testing (i.e., DFT and general kinetic models), are required to facilitate the preparation of catalysts and to investigate the energetics of intermediates at various points within the catalytic structure through mechanism studies. Throughout the catalytic process, the catalyst's deactivation and stability will be taken into account. Finally, for the development of catalysts with high CO₂ conversion rates and high CO selectivity, we can proceed based on the following aspects: (1) improving the preparation method for catalysts to improve the dispersion of active components and (2) modifying the carrier to increase the dispersion of metal species and adjust the interaction between the active component and the carrier. In addition, we may be able to promote the development of low-carbon industrial catalysis using light-driven chemical reactions and develop and design suitable catalysts to gradually transition RWGS reactions from thermal reactions to photocatalytic processes.

Author Contributions: Writing—original draft, C.Z., J.Z. and Y.F. Writing—review and editing, H.D. All authors have read and agreed to the published version of the manuscript.

Funding: This research was funded by support from the 2023 Jiangsu Degree and Postgraduate Education Teaching Reform project (JGKT23_C085), the 2023 Jiangsu Graduate Research and Practice Innovation plan (KYCX23_3469), the Funding for School-level Research projects of Yancheng Institute of Technology (No. xjr2019007 and No. xjr2023031), the 2023 Excellent Graduation Project (Thesis) Cultivation project of Yancheng Institute of Technology, and the Natural Science Foundation of Sichuan (No. 2023NSFSC1103).

Institutional Review Board Statement: Not applicable.

Informed Consent Statement: Not applicable.

Data Availability Statement: Data are contained within the review.

Conflicts of Interest: The authors declare no conflict of interest.

References

1. Tawalbeh, M.; Javed, R.M.N.; Al-Othman, A.; Almomani, F. The novel contribution of non-noble metal catalysts for intensified carbon dioxide hydrogenation. *Energy Convers. Manag.* **2023**, *279*, 116755. [[CrossRef](#)]
2. Yao, X.; Zhong, P.; Zhang, X.; Zhu, L. Business model design for the carbon capture utilization and storage (CCUS) project in China. *Energy Policy* **2018**, *121*, 519. [[CrossRef](#)]
3. Tapia, J.F.D.; Lee, J.; Ooi, R.E.H.; Foo, D.C.Y.; Tan, R.R. A review of optimization and decision-making models for the planning of CO₂ capture, utilization and storage (CCUS) systems. *Sustain. Prod. Consump.* **2018**, *13*, 1. [[CrossRef](#)]
4. Adelung, S.; Dietrich, R.U. Impact of the reverse water gas shift operating conditions on the Power-to-Liquid fuel production cost. *Fuel* **2022**, *317*, 123440. [[CrossRef](#)]
5. Atspha, T.A.; Yoon, T.; Seongho, P.; Lee, C. A review on the catalytic conversion of CO₂ using H₂ for synthesis of CO, methanol, and hydrocarbons. *J. CO₂ Util.* **2021**, *44*, 101413. [[CrossRef](#)]
6. Lima, D.D.S.; Dias, Y.R.; Pere z-Lopez, O.W. CO₂ methanation over Ni-Al and Co-Al LDH-derived catalysts: The role of basicity. *Sustain. Energy Fuels* **2020**, *4*, 5747. [[CrossRef](#)]
7. Abdel-Mageed, A.M.; Wiese, K.; Parlinska-Wojtan, M.; Rabeah, J.; Behma, A.; Brückner, J.R. Encapsulation of Ru nanoparticles: Modifying the reactivity toward CO and CO₂ methanation on highly active Ru/TiO₂ catalysts. *Appl. Catal. B-Environ.* **2020**, *270*, 118846. [[CrossRef](#)]
8. Dai, H.; Xiong, S.; Zhu, Y.; Zheng, J.; Huang, L.; Zhou, C.; Deng, J.; Zhang, X. NiCe bimetallic nanoparticles embedded in hexagonal mesoporous silica (HMS) for reverse water gas shift reaction. *Chin. Chem. Lett.* **2022**, *33*, 2590. [[CrossRef](#)]
9. Dai, H.; Zhang, A.; Xiong, S.; Xiao, X.; Zhou, C.; Pan, Y. The Catalytic Performance of Ga₂O₃-CeO₂ Composite Oxides over Reverse Water Gas Shift Reaction. *ChemCatChem* **2022**, *14*, e202200049. [[CrossRef](#)]
10. Zhao, J.; Shi, R.; Waterhouse, G.I.N.; Zhang, T. Selective photothermal CO₂ reduction to CO, CH₄, alkanes, alkenes over bimetallic alloy catalysts derived from layered double hydroxide nanosheets. *Nano Energy* **2022**, *102*, 107650. [[CrossRef](#)]
11. Xie, B.; Lovell, E.; Tan, T.H.; Jantarang, S.; Yu, M.; Scott, J.; Amal, R. Emerging material engineering strategies for amplifying photothermal heterogeneous CO₂ catalysis. *J. Energy Chem.* **2021**, *59*, 108. [[CrossRef](#)]
12. Zeng, X.; Tu, Z.; Yuan, L.; Xiao, C.; Wen, Y.; Xiong, K. Two-Dimensional transition metal hexaaminobenzene monolayer single atom catalyst for electrocatalytic Carbon Dioxide Reduction. *Nanomaterials* **2022**, *12*, 4005. [[CrossRef](#)]

13. Xue, R.; Ge, P.; Xie, J.; Hu, Z.Y.; Wang, X.K.; Li, P.Q. Controllable CO₂ reduction or hydrocarbon oxidation driven by entire solar via silver quantum dots direct photocatalysis. *Small* **2023**, *19*, 2207234. [[CrossRef](#)]
14. Porosoff, M.D.; Yan, B.H.; Chen, J.G.G. Catalytic reduction of CO₂ by H₂ for synthesis of CO, methanol and hydrocarbons: Challenges and opportunities. *Energy Environ. Sci.* **2016**, *9*, 62–73. [[CrossRef](#)]
15. Portillo, E.; Gandara, J.; Reina, T.R.; Pastor-Perez, L. Is the RWGS a viable route for CO₂ conversion to added value products? A techno-economic study to understand the optimal RWGS conditions. *Sci. Total Environ.* **2023**, *857*, 159394. [[CrossRef](#)]
16. Alvarez-Galvan, C.; Lustemberg, P.G.; Oropeza, F.E.; Bashiller-Baeza, B.; Ospina, M.D.; Herranz, M.; Cebollada, J.; Collado, L.; Campos-Martin, J.M.; Pena-O'Shea, V.A.; et al. Highly active and stable Ni/La-doped ceria material for catalytic CO₂ reduction by reverse water gas shift reaction. *ACS Appl. Mater. Inter.* **2022**, *14*, 50739. [[CrossRef](#)] [[PubMed](#)]
17. Ranjbar, A.; Irankhah, A.; Aghamiri, S.F. Reverse water gas shift reaction and CO₂ mitigation: Nanocrystalline MgO as a support for nickel based catalysts. *J. Environ. Chem. Eng.* **2018**, *6*, 4945. [[CrossRef](#)]
18. Petersen, E.M.; Rao, R.G.; Vance, B.C.; Tessonier, J.P. SiO₂/SiC supports with tailored thermal conductivity to reveal the effect of surface temperature on Ru-catalyzed CO₂ methanation. *Appl. Catal. B-Environ.* **2021**, *286*, 119904. [[CrossRef](#)]
19. Li, S.; Liu, G.; Zhang, S.; An, K.; Ma, Z.; Wang, L.; Liu, Y. Cerium modified Ni-La₂O₃/ZrO₂ for CO₂ methanation. *J. Energy Chem.* **2020**, *43*, 155. [[CrossRef](#)]
20. Zhang, F.; Liu, Z.Y.; Chen, X.B.; Rui, N.; Betancourt, L.E.; Lin, L.L.; Xu, W.Q.; Sun, C.J.; Abeykoon, A.M.M.; Rodriguez, J.A.; et al. Effects of Zr doping into ceria for the dry reforming of methane over Ni/CeZrO₂ catalysts: In situ studies with XRD, XAFS, and AP-XPS. *ACS Catal.* **2020**, *10*, 3274. [[CrossRef](#)]
21. Martin, O.; Antonio, J.M.; Cecilia, M.; Sharon, M.; Takuya, F.S.; Roland, H.; Charlotte, D.; Daniel, C.F.; Javier, P.R. Indium oxide as a superior catalyst for methanol synthesis by CO₂ hydrogenation. *Angew. Chem. Int. Ed.* **2016**, *55*, 6261. [[CrossRef](#)]
22. Chen, K.H.; Li, H.R.; He, L.N. Advance and prospective on CO₂ activation and transformation strategy. *Chin. J. Org. Chem.* **2020**, *40*, 2195. [[CrossRef](#)]
23. Panagiotopoulou, P. Hydrogenation of CO₂ over supported noble metal catalysts. *Appl. Catal. A-Gen* **2017**, *542*, 63. [[CrossRef](#)]
24. Daza, Y.A.; Kuhn, J.N. CO₂ conversion by reverse water gas shift catalysis: Comparison of catalysts, mechanisms and their consequences for CO₂ conversion to liquid fuels. *RSC Adv.* **2016**, *6*, 49675. [[CrossRef](#)]
25. Su, X.; Yang, X.L.; Zhao, B.; Huang, Y.Q. Designing of highly selective and high-temperature endurable RWGS heterogeneous catalysts: Recent advances and the future directions. *J. Energy Chem.* **2017**, *26*, 854. [[CrossRef](#)]
26. Bahmanpour, A.M.; Signorile, M.; Kröcher, O. Recent progress in syngas production via catalytic CO₂ hydrogenation reaction. *Appl. Catal. B-Environ.* **2021**, *295*, 120319. [[CrossRef](#)]
27. Ebrahimi, P.; Kumar, A.; Khraisheh, M. A Review of CeO₂ Supported Catalysts for CO₂ Reduction to CO through the Reverse Water Gas Shift Reaction. *Catalysts* **2022**, *12*, 1101. [[CrossRef](#)]
28. Pahija, E.; Panaritis, C.; Gusarov, S.; Shadbahr, J.; Bensebaa, F.; Patience, G.; Boffito, D.C. Experimental and Computational Synergistic Design of Cu and Fe Catalysts for the Reverse Water-Gas Shift: A Review. *ACS Catal.* **2022**, *12*, 6887. [[CrossRef](#)]
29. Abdel-Mageed, A.L.; Wohlrab, S. Review of CO₂ Reduction on Supported Metals (Alloys) and Single-Atom Catalysts (SACs) for the Use of Green Hydrogen in Power-to-Gas Concepts. *Catalysts* **2022**, *12*, 16. [[CrossRef](#)]
30. Jing, H.; Li, Q.; Wang, J.; Liu, D.; Wu, K. Theoretical Study of the Reverse Water Gas Shift Reaction on Copper Modified β-Mo₂C(001) Surfaces. *J. Phys. Chem. C.* **2019**, *123*, 1235. [[CrossRef](#)]
31. Lin, L.; Yao, S.; Liu, Z.; Zhang, F.; Li, N.; Vovchok, D.; Martinez-Arias, A.; Castañeda, R.; Lin, J.; Senanayake, S.D. In situ characterization of Cu/CeO₂ nanocatalysts for CO₂ hydrogenation: Morphological effects of nanostructured ceria on the catalytic activity. *J. Phys. Chem. C.* **2018**, *122*, 12934. [[CrossRef](#)]
32. Mine, S.; Yamaguchi, T.; Ting, K.W.; Maeno, Z.; Siddiki, S.M.A.H.; Oshima, K.; Satokawa, S.; Shimizu, K.; Toyao, T. Reverse water-gas shift reaction over Pt/MoO_x/TiO₂: Reverse Mars-van Krevelen mechanism via redox of supported MoO_x. *Catal. Sci. Technol.* **2021**, *11*, 4172. [[CrossRef](#)]
33. Liu, Y.; Li, Z.; Xu, H.; Han, Y. Reverse water-gas shift reaction over ceria nanocube synthesized by hydrothermal method. *Catal. Commun.* **2016**, *76*, 1. [[CrossRef](#)]
34. Lu, B.; Zhang, T.; Zhang, L.; Xu, Y.; Zhang, Z.; Wu, F.; Li, X.; Luo, C. Promotion effects of oxygen vacancies on activity of Na-doped CeO₂ catalysts for reverse water gas shift reaction. *Appl. Surf. Sci.* **2022**, *587*, 152881. [[CrossRef](#)]
35. Li, M.; My Pham, T.H.; Ko, Y.; Zhao, K.; Zhong, L.; Luo, W.; Züttel, A. Support-Dependent Cu-In Bimetallic Catalysts for Tailoring the Activity of Reverse Water Gas Shift Reaction. *ACS Sustain. Chem. Eng.* **2022**, *10*, 1524. [[CrossRef](#)]
36. Gines, M.J.L.; Marchi, A.J.; Apesteguía, C.R. Kinetic study of the reverse water gas shift reaction over CuO/ZnO/Al₂O₃ catalysts. *Appl. Catal. A-Gen.* **1997**, *154*, 15. [[CrossRef](#)]
37. Wang, L.C.; Khazaneh, M.T.; Widmann, D.; Behm, R.J. TAP reactor studies of the oxidizing capability of CO₂ on a Au/CeO₂ catalyst—A first step toward identifying a redox mechanism in the reverse water gas shift reaction. *J. Catal.* **2013**, *302*, 20. [[CrossRef](#)]
38. Liu, H.X.; Li, S.Q.; Wang, W.W.; Yu, W.Z.; Zhang, W.J.; Ma, C.; Jia, C.J. Partially sintered copper-ceria as excellent catalyst for the high temperature reverse water gas shift reaction. *Nat. Commun.* **2022**, *13*, 867. [[CrossRef](#)]
39. Deng, L.; Su, Q.Q.; Ye, Q.; Wan, H.; He, Y.; Cui, X. Slag-based geopolymer microsphere-supported Cu: A low cost and sustainable catalyst for CO₂ hydrogenation. *Sustain. Energy Fuels* **2022**, *6*, 1436. [[CrossRef](#)]

40. Matsubu, J.C.; Zhang, S.; Derita, L.; Marinkovic, N.S.; Chen, J.G.; Graham, G.W.; Pan, X.; Christopher, P. Adsorbate mediated strong metal support interactions in oxide supported Rh catalysts. *Nat. Chem.* **2017**, *9*, 120. [\[CrossRef\]](#)
41. Li, W.; Gan, J.; Liu, Y.; Zou, Y.; Zhang, S.; Qu, Y. Platinum and Frustrated Lewis Pairs on Ceria as Dual-Active Sites for Efficient Reverse Water-Gas Shift Reaction at Low Temperatures. *Angew. Chem. Int. Ed.* **2023**, *62*, e202305661. [\[CrossRef\]](#) [\[PubMed\]](#)
42. Chen, X.; Su, X.; Liang, B.; Yang, X.; Ren, X.; Duan, H.; Huang, Y.; Zhang, T. Identification of relevant active sites and a mechanism study for reverse water gas shift reaction over Pt/CeO₂ catalysts. *J. Energy Chem.* **2016**, *25*, 1051. [\[CrossRef\]](#)
43. Liu, Y.X.; Li, L.W.; Zhang, R.Y.; Guo, Y.H.; Wang, H.; Ge, Q.F.; Zhu, X.L. Synergetic enhancement of activity and selectivity for reverse water gas shift reaction on Pt-Re/SiO₂ catalysts. *J. CO₂ Util.* **2022**, *63*, 102128. [\[CrossRef\]](#)
44. Bhalothia, D.; Yang, S.S.; Yan, C.; Beniwal, A.; Chang, Y.X.; Wu, S.C.; Chen, P.C.; Wang, K.W.; Chen, T.Y. Surface anchored atomic cobalt-oxide species coupled with oxygen vacancies boost the CO-production yield of Pd nanoparticles. *Sustain. Energy Fuels* **2023**, *7*, 526. [\[CrossRef\]](#)
45. Abdel-Mageed, A.; Wiese, K.; Hauble, A.; Bansmann, J.; Rabeah, J.; Parlinska-Wojtan, M.; Bruckner, A.; Behm, R. Steering the selectivity in CO₂ reduction on highly active Ru/TiO₂ catalysts: Support particle size effects. *J. Catal.* **2021**, *401*, 160. [\[CrossRef\]](#)
46. Vikanova, K.V.; Kustov, A.L.; Makhov, E.A.; Tkachenko, O.P.; Kapustin, G.I.; Kalmykov, K.B.; Mishin, I.V.; Nissenbaum, V.D.; Dunaev, S.F.; Kustov, L.M. Rhenium-contained catalysts based on superacid ZrO₂ supports for CO₂ utilization. *Fuel* **2023**, *351*, 128956. [\[CrossRef\]](#)
47. Rabeah, A.; Zhao, D.; Cisneros, S.; Kreyenschulte, C.R.; Kondratenko, V.; Bartling, S.; Kubis, C.; Kondratenko, E.I.V.; Brückner, A.; Rabeah, J. Role of interfacial oxygen vacancies in low loaded Au-based catalysts for the low temperature reverse water gas shift reaction. *Appl. Catal. B-Env.* **2023**, *321*, 122083. [\[CrossRef\]](#)
48. Zhang, Z.Y.; Zang, Y.H.; Gao, F.; Qu, J.F.; Gu, J.F.; Lin, X.T. Enhanced catalytic activity of CO₂ hydrogenation to CO over sulfur-containing Ni/ZrO₂ catalysts: Support size effect. *New J. Chem.* **2022**, *46*, 22332. [\[CrossRef\]](#)
49. Kim, Y.; Kim, K.; Song, Y.; Lee, Y.; Roh, H.; Na, K. Highly CO-selective Ni-MgO-Ce_xZr_{1-x}O₂ catalyst for efficient low-temperature reverse water-gas shift reaction. *J. Ind. Eng. Chem.* **2023**, *118*, 341. [\[CrossRef\]](#)
50. Kim, D.H.; Han, S.W.; Yoon, H.S.; Kim, Y.D. Reverse water gas shift reaction catalyzed by Fe nanoparticles with high catalytic activity and stability. *J. Ind. Eng. Chem.* **2015**, *23*, 67. [\[CrossRef\]](#)
51. Zhuang, Y.; Currie, R.; McAuley Kimberley, B.; Simakov, D.S.A. Highly-selective CO₂ conversion via reverse water gas shift reaction over the 0.5wt% Ru-promoted Cu/ZnO/Al₂O₃ catalyst. *Appl. Catal. A-Gen.* **2019**, *575*, 74. [\[CrossRef\]](#)
52. Ebrahimi, P.; Kumar, A.; Khraisheh, M. Combustion synthesis of copper ceria solid solution for CO₂ conversion to CO via reverse water gas shift reaction. *Int. J. Hydrogen Energy* **2022**, *47*, 41259. [\[CrossRef\]](#)
53. Zhang, L.; Yu, J.; Sun, X.; Sun, J. Engineering nanointerfaces of Cu-based catalysts for balancing activity and stability of reverse water gas shift reaction. *J. CO₂ Util.* **2023**, *71*, 102460. [\[CrossRef\]](#)
54. Zhang, R.; Wei, A.; Zhu, M.; Wu, X.X.; Wang, H.; Zhu, X.L.; Ge, Q.F. Tuning reverse water gas shift and methanation reactions during CO₂ reduction on Ni catalysts via surface modification by MoO_x. *J. CO₂ Util.* **2021**, *52*, 101678. [\[CrossRef\]](#)
55. Okemoto, A.; Harada, M.R.; Ishizaka, T.; Hiyoshi, N.; Soto, K. Catalytic performance of MoO₃/FAU zeolite catalysts modified by Cu for reverse water gas shift reaction. *Appl. Catal. A Gen.* **2020**, *592*, 117415. [\[CrossRef\]](#)
56. Ronda-lloret, M.; Yang, L.Q.Q.; Hammerton, M.; Marakatti, V.S.; Tromp, M.; Sofer, Z.; Sepulveda-Escribano, A.; Ramos-Fernandez, E.V.; Delgado, J.J.; Rothenberg, G.; et al. Molybdenum oxide supported on Ti₃AlC₂ is an active reverse water gas shift catalyst. *ACS Sustain. Chem. Eng.* **2021**, *9*, 4957.
57. Kharaji, A.G.; Shariati, A.; Takassi, M. A novel γ -Alumina supported Fe-Mo bimetallic catalyst for reverse water gas shift reaction. *Chin. J. Chem. Eng.* **2013**, *21*, 1007. [\[CrossRef\]](#)
58. Yang, L.; Pastor-perez, L.; Gu, S.; Sepúlveda-Escribano, A.; Reina, T.R. Highly efficient Ni/CeO₂-Al₂O₃ catalysts for CO₂ upgrading via reverse water gas shift: Effect of selected transition metal promoters. *Appl. Catal. B-Environ.* **2018**, *232*, 464. [\[CrossRef\]](#)
59. Goguet, A.; Meunier, F.; Breen, J.; Burch, R.; Petch, M.; Faurghenciu, A. Study of the origin of the deactivation of a Pt/CeO₂ catalyst during reverse water gas shift (RWGS) reaction. *J. Catal.* **2004**, *226*, 382. [\[CrossRef\]](#)
60. Lymperi, A.; Chatziliadis, C.; Xydias, F.; Martino, E.; Kyriakou, G.; Katsaounis, A. Electrochemical Promotion of CO₂ Hydrogenation Using a Pt/YSZ Fuel Cell Type Reactor. *Nanomaterials* **2023**, *13*, 1930. [\[CrossRef\]](#)
61. Seuser, G.; Martinelli, M.; Garcia, E.S.; Upton, G.F.; Ayala, M.; Villarreal, J.; Rajabi, Z.; Cronauer, D.C.; Kropf, A.J.; Jacobs, G. Reverse water-gas shift: Na doping of m-ZrO₂ supported Pt for selectivity control. *Appl. Catal. A-Gen.* **2023**, *650*, 119000. [\[CrossRef\]](#)
62. Ge, H.; Kuwahara, Y.; Kusu, K.; Kobayashi, H.; Yamashita, H. Enhanced visible-NIR absorption and oxygen vacancy generation of Pt/H_xMoWO_y by H-spillover to facilitate photothermal catalytic CO₂ hydrogenation. *J. Mater. Chem. A* **2022**, *10*, 10854. [\[CrossRef\]](#)
63. He, Y.L.; Huang, D.H. Single-Atom Platinum Catalyst for Efficient CO₂ Conversion via Reverse Water Gas Shift Reaction. *Molecules* **2023**, *28*, 6630. [\[CrossRef\]](#)
64. Nelson, N.C.; Chen, L.X.; Meira, D.; Kovarik, L.; Szanyi, J. In situ dispersion of palladium on TiO₂ during reverse water gas shift reaction: Formation of atomically dispersed palladium. *Angew. Chem. Int. Ed.* **2020**, *59*, 17657. [\[CrossRef\]](#) [\[PubMed\]](#)
65. Onodera, T.; Miyake, T.; Sugimasaa, M. Low-temperature RWGS enhancement of Pt₁-nAu_n/CeO₂ catalysts and their electronic state. *RSC Adv.* **2023**, *13*, 29320. [\[CrossRef\]](#) [\[PubMed\]](#)

66. Du, P.; Qi, R.; Zhang, Y.; Gu, Q.; Xu, X.; Tan, Y.; Liu, X.; Wang, A.; Zhu, B.; Yang, B.; et al. Single-atom-driven dynamic carburization over Pd1-FeOx catalyst boosting CO₂ conversion. *Chem* **2022**, *8*, 3252. [CrossRef]
67. Yang, Z.; Zhao, T.; Tang, Y.; Jiang, Y.; Kitagawa, H.; Wen, X.; Wang, F. Size-modulated photo-thermal catalytic CO₂ hydrogenation performances over Pd nanoparticles. *J. Catal.* **2023**, *424*, 22. [CrossRef]
68. Chen, L.; Allec, S.I.; Nguyen, M.T.; Kovarik, L.; Hoffman, A.S.; Hong, J.; Meira, D.; Shi, H.; Bare, S.R.; Glezakou, V.A.; et al. Dynamic Evolution of Palladium Single Atoms on Anatase Titania Support Determines the Reverse Water-Gas Shift Activity. *J. Am. Chem. Soc.* **2023**, *145*, 10847. [CrossRef]
69. Ni, W.; Zeng, M.; Wang, K.; Lin, Y.; Zhang, Z.; Dai, W.; Fu, X. Photo-thermal catalytic reverse water gas shift reaction over Pd/MaZrO_x (M= Sr, SrMn) catalysts driven by Cycle-double sites. *J. CO₂ Util.* **2023**, *69*, 102413. [CrossRef]
70. Saravanan, P.K.; Bhalothia, D.; Huang, G.H.; Beniwal, A.; Cheng, M.; Chao, Y.C.; Lin, M.W.; Chen, P.C.; Chen, T.Y. Sub-Millisecond Laser-Irradiation-Mediated Surface Restructure Boosts the CO Production Yield of Cobalt Oxide Supported Pd Nanoparticles. *Nanomaterials* **2023**, *13*, 1801. [CrossRef]
71. Zhang, R.; Wang, X.; Wang, K.; Wang, H.; Liu, L.; Wu, X.; Geng, B.; Chu, X.; Song, S.; Zhang, H. Synergism of Ultrasmall Pt Clusters and Basic La₂O₂CO₃ Supports Boosts the Reverse Water Gas Reaction Efficiency. *Adv. Energy Mater.* **2023**, *13*, 2203806. [CrossRef]
72. Tang, R.; Zhu, Z.; Li, C.; Xiao, M.Q.; Wu, Z.Y.; Zhang, D.K.; Zhang, C.C.; Xiao, Y.; Chu, M.Y.; Genest, A.; et al. Ru-catalyzed reverse water gas shift reaction with near unity selectivity and superior stability. *ACS Mater. Lett.* **2021**, *3*, 1652. [CrossRef] [PubMed]
73. Wu, Z.; Shen, J.; Li, C.; Zhang, C.; Feng, K.; Wang, Z.; Wang, X.; Meira, D.M.; Cai, M.; Zhang, D.; et al. Mo₂TiC₂ MXene-Supported Ru Clusters for Efficient Photothermal Reverse Water-Gas Shift. *ACS Nano*. **2023**, *17*, 1550. [CrossRef] [PubMed]
74. Chen, L.; Pilot, I.A.W.; Hensen, E.J.M. Elucidation of the Reverse Water-Gas Shift Reaction Mechanism over an Isolated Ru Atom on CeO₂(111). *J. Phys. Chem. C* **2023**, *127*, 20314. [CrossRef]
75. Kim, G.; Shin, S.; Choi, Y.; Kim, J.; Kim, G.; Kim, K.; Lee, H. Gas-Permeable Iron-Doped Ceria Shell on Rh Nanoparticles with High Activity and Durability. *JACS Au*. **2022**, *2*, 1115. [CrossRef] [PubMed]
76. Wang, K.; Shao, S.; Liu, Y.; Cao, M.; Yu, J.; Lau, C.H.; Zheng, Y.; Fan, X. DRIFTS-SSITKA-MS investigations on the mechanism of plasmon preferentially enhanced CO₂ hydrogenation over Au/ γ -Al₂O₃. *Appl. Catal. B-Environ.* **2023**, *328*, 122531. [CrossRef]
77. Kang, X.; Yuan, D.; Yi, Z.; Yu, C.; Yuan, X.; Liang, B.; Sun, X.; Gao, L.; Wang, S.; Li, Y. Bismuth single atom supported CeO₂ nanosheets for oxidation resistant photothermal reverse water gas shift reaction. *Catal. Sci. Technol.* **2022**, *12*, 5559. [CrossRef]
78. Yang, B.; Wang, Y.; Gao, B.; Zhang, L.; Guo, L. Size-Dependent Active Site and Its Catalytic Mechanism for CO₂ Hydrogenation Reactivity and Selectivity over Re/TiO₂. *ACS Catal.* **2023**, *13*, 10364. [CrossRef]
79. Liu, Y.; Chen, J.; Mou, L.; Liu, Q.; Li, Z.; Li, X.; He, S. Reverse water-gas shift reaction catalyzed by diatomic rhodium anions. *Phys. Chem. Chem. Phys.* **2022**, *24*, 14616. [CrossRef]
80. Lu, J.; Zhang, S.; Zhou, H.; Huang, C.; Xia, L.; Liu, X.; Luo, H.; Wang, H. Ir Single Atoms and Clusters Supported on α -MoC as Catalysts for Efficient Hydrogenation of CO₂ to CO. *Acta Phys-Chim. Sin.* **2023**, *39*, 230202.
81. Mhamane, N.B.; Chetry, S.; Ranjan, R.; Raja, T.; Gopinath, C.S. Sustainable CO₂ Reduction on In₂O₃ with Exclusive CO Selectivity: Catalysis and In Situ Valence Band Photoelectron Spectral Investigations. *ACS Sustain. Chem. Eng.* **2022**, *10*, 3521. [CrossRef]
82. Gong, J.; Chu, M.Y.; Guan, W.H.; Liu, Y.; Zhong, Q.X.; Cao, M.H.; Xu, Y. Regulating the interfacial synergy of Ni/Ga₂O₃ for CO₂ hydrogenation toward the reverse water gas shift reaction. *Ind. Eng. Chem. Res.* **2021**, *60*, 9448. [CrossRef]
83. Zhang, Q.; Pastor-Pérez, L.; Villora-Pico, J.J.; Joyce, M.; Sepúlveda-Escribano, A.; Duyar, M.S.; Reina, T.R. Ni-Phosphide catalysts as versatile systems for gas-phase CO₂ conversion: Impact of the support and evidences of structure-sensitivity. *Fuel* **2022**, *323*, 124301. [CrossRef]
84. Shen, H.; Dong, Y.; Yang, S.; He, Y.; Wang, Q.; Cao, Y.; Wang, W.; Wang, T.; Zhang, Q.; Zhang, H. Identifying the roles of Ce³⁺-OH and Ce-H in the reverse water-gas shift reaction over highly active Ni-doped CeO₂ catalyst. *Nano Res.* **2022**, *15*, 5831. [CrossRef]
85. Ranjbar, A.; Aghamiri, S.F.; Irankhah, A. Effect of MgO/Al₂O₃ ratio in the support of mesoporous Ni/MgO-Al₂O₃ catalysts for CO₂ utilization via reverse water gas shift reaction. *Int. J. Hydrogen Energy* **2023**, *48*, 19115. [CrossRef]
86. Zagoraios, D.; Kokkinou, N.; Kyriakou, G.; Katsaounis, A. Electrochemical control of the RWGS reaction over Ni nanoparticles deposited on yttria stabilized zirconia. *Catal. Sci. Technol.* **2022**, *12*, 1869. [CrossRef]
87. Lozano-Reis, P.; Prats, H.; Sayós, R.; Illas, F. Limitations of free energy diagrams to predict the catalytic activity: The reverse water gas shift reaction catalyzed by Ni/TiC. *J. Catal.* **2023**, *425*, 203. [CrossRef]
88. Rutherford, B.; Panaritis, C.; Pahija, E.; Couillard, M.; Patarachao, B.; Shadbahr, J.; Bensebaa, F.; Patience, G.S.; Boffito, D.C. Ni nanoparticles on Co₃O₄ catalyze the reverse water-gas shift with 95% CO selectivity at 300 °C. *Fuel* **2023**, *348*, 128235. [CrossRef]
89. Wang, D.; Yuan, Z.; Wu, X.; Xiong, W.; Ding, J.; Zhuang, Z.; Huang, W. Ni Single Atoms Confined in Nitrogen-Doped Carbon Nanotubes for Active and Selective Hydrogenation of CO₂ to CO. *ACS Catal.* **2023**, *13*, 7132. [CrossRef]
90. Chen, C.; Chen, H.; Huang, C.; Chen, C.; Choojun, K.; Sooknoi, T.; Tian, H.; Lin, Y. Reversal of methanation-oriented to RWGS-oriented Ni/SiO₂ catalysts by the exsolution of Ni²⁺ confined in silicalite-1. *Green Chem.* **2023**, *25*, 7582. [CrossRef]
91. Wei, A.; Zhang, R.; Qin, Y.; Wang, H.; Zhu, X.; Ge, Q. Theoretical Insight into Tuning CO₂ Methanation and Reverse Water Gas Shift Reactions on MoO^x-Modified Ni Catalysts. *J. Phys. Chem. C* **2022**, *126*, 18078. [CrossRef]
92. Arpini, B.H.; Braga, A.H.; Borges, L.R.; Vidinha, P.; Gonçalves, R.V.; Szanyi, J.; Rossi, L.M. Tuning CO₂ Hydrogenation Selectivity by N-Doped Carbon Coating over Nickel Nanoparticles Supported on SiO₂. *ACS Sustain. Chem. Eng.* **2022**, *10*, 2331. [CrossRef]

93. Wang, Y.; Chen, J.; Chen, L.; Li, Y. Breaking the Linear Scaling Relationship of the Reverse Water-Gas-Shift Reaction via Construction of Dual-Atom Pt-Ni Pairs. *ACS Catal.* **2023**, *13*, 3735. [[CrossRef](#)]
94. Błaszczak, P.; Zając, M.; Ducka, A.; Matlak, K.; Wolanin, B.; Wang, S.; Mandziak, A.; Bochentyn, B.; Jasiński, P. High-temperature Co-electrolysis of CO₂/H₂O and direct methanation over Co-impregnated SOEC. Bimetallic synergy between Co and Ni. *Int. J. Hydrogen Energy* **2022**, *47*, 35017. [[CrossRef](#)]
95. Merkouri, L.; Saché, E.; Pastor-Pérez, L.; Duyar, M.S.; Reina, T.R. Versatile Ni-Ru catalysts for gas phase CO₂ conversion: Bringing closer dry reforming, reverse water gas shift and methanation to enable end-products flexibility. *Fuel* **2022**, *315*, 123097. [[CrossRef](#)]
96. Zhang, C.; Zhang, R.; Liu, Y.; Wu, X.; Wang, H.; Ge, Q.; Zhu, X. Blocking Methanation during Reverse Water Gas Shift Reaction on Ni/SiO₂ Catalysts by Surface Ag. *ChemCatChem* **2022**, *15*, e202201284. [[CrossRef](#)]
97. Guo, J.; Wang, Z.; Li, J.; Wang, Z. In-Ni Intermetallic Compounds Derived from Layered Double Hydroxides as Efficient Catalysts toward the Reverse Water Gas Shift Reaction. *ACS Catal.* **2022**, *12*, 4026. [[CrossRef](#)]
98. Cai, W.; Yin, J.; Hu, C.; Han, H.; Ma, J.; Cao, Y.; Zhao, Y. Fe-Co-Ni Trimetallic Catalysts with MOFs as Precursor for CO₂ Hydrogenation to C₂-C₄ Hydrocarbons: Insight Into the Influence of Ni. *Catal Lett.* **2023**, *153*, 2718. [[CrossRef](#)]
99. Bogdan, V.I.; Koklin, A.E.; Kustov, A.L.; Pokusaeva, Y.A.; Bogdan, T.V.; Kustov, L.M. Carbon Dioxide Reduction with Hydrogen on Fe, Co Supported Alumina and Carbon Catalysts under Supercritical Conditions. *Molecules* **2021**, *26*, 2883. [[CrossRef](#)]
100. Zhang, Q.; Pastor-perez, L.; Wang, Q.; Reina, T.R. Conversion of CO₂ to added value products via rwgs using Fe-promoted catalysts: Carbide, metallic Fe or a mixture. *Energy Chem.* **2022**, *66*, 635. [[CrossRef](#)]
101. Watanabe, R.; Karasawa, F.; Yokoyama, C.; Oshima, K.; Kishida, M.; Hori, M.; Ono, Y.; Satokawa, S.; Verma, P.; Fukuhara, C. Highly stable Fe/CeO₂ catalyst for the reverse water gas shift reaction in the presence of H₂S. *RSC Adv.* **2023**, *13*, 11525. [[CrossRef](#)]
102. Xu, M.; Cao, C.; Xu, J. Understanding kinetically interplaying reverse water-gas shift and Fischer-Tropsch synthesis during CO₂ hydrogenation over Fe-based catalysts. *Appl. Catal. A-Gen.* **2022**, *641*, 118682. [[CrossRef](#)]
103. Malhi, H.S.; Sun, C.; Zhang, Z.; Liu, Y.; Liu, W.; Ren, P.; Tu, W.; Han, Y. Catalytic consequences of the decoration of sodium and zinc atoms during CO₂ hydrogenation to olefins over iron-based catalyst. *Catal. Today* **2022**, *387*, 28. [[CrossRef](#)]
104. Fedorov, A.; Lund, H.; Kondratenko, V.A.; Kondratenko, E.V.; Linke, D. Elucidating reaction pathways occurring in CO₂ hydrogenation over Fe-based catalysts. *Appl. Catal. B-Environ.* **2023**, *328*, 122505. [[CrossRef](#)]
105. Panek, B.; Kierzkowska-Pawlak, H.; Uznański, P.; Nagy, S.; Nagy-Trembošová, V.; Tyczkowski, J. The Role of Carbon Nanotube Deposit in Catalytic Activity of FeO^X-Based PECVD Thin Films Tested in RWGS Reaction. *Catalysts* **2023**, *13*, 1302. [[CrossRef](#)]
106. Ai, X.; Xie, H.; Chen, S.; Zhang, G.; Xu, B.; Zhou, G. Highly dispersed mesoporous Cu/ γ -Al₂O₃ catalyst for RWGS reaction. *Int. J. Hydrogen Energy* **2022**, *47*, 14884. [[CrossRef](#)]
107. Liu, C.; Nauert, S.L.; Alsina, M.A.; Wang, D.; Grant, A.; He, K.; Weitz, E.; Nolan, M.; Gray, K.A.; Notestein, J.M. Role of surface reconstruction on Cu/TiO₂ nanotubes for CO₂ conversion. *Appl. Catal. B Env.* **2019**, *255*, 117754. [[CrossRef](#)]
108. Gonzalez-arias, J.; Gonzalez-Castano, M.; Sanchez, M.E.; Cara-Jimenez, J.; Arellano-Garcia, H. Valorization of biomass-derived CO₂ residues with Cu-MnO_x catalysts for RWGS reaction. *Renew. Energy* **2022**, *182*, 443. [[CrossRef](#)]
109. Yang, Z.; Zeng, M.; Wang, K.; Yue, X.; Chen, X.; Dai, W.; Fu, X. Visible light-assisted thermal catalytic reverse water gas reaction over Cu-CeO₂: The synergistic of hot electrons and oxygen vacancies induced by LSPR effect. *Fuel* **2022**, *315*, 123186. [[CrossRef](#)]
110. Dehghanpoor, S.; Sedaghat, M.H.; Bakhtyari, A.; Makarem, M.A.; Rahimpour, M.R. A Feasibility Study of the Conversion of Petrochemical Off-Gas Streams to Methanol Over CuO/ZnO/Al₂O₃ Catalyst. *Top. Catal.* **2022**. [[CrossRef](#)]
111. Xiong, W.; Wu, Z.; Chen, X.; Ding, J.; Ye, A.; Zhang, W.; Huang, W. Active copper structures in ZnO-Cu interfacial catalysis: CO₂ hydrogenation to methanol and reverse water-gas shift reactions. *Sci. China Chem.* **2023**. [[CrossRef](#)]
112. Ebrahimi, P.; Kumar, A.; Khraisheh, M. Combustion synthesis of lanthanum oxide supported Cu, Ni, and CuNi nanoparticles for CO₂ conversion reaction. *Int. J. Hydrogen Energy* **2023**, *48*, 24580. [[CrossRef](#)]
113. Zhang, S.; Chen, L.; Pan, W.B.; Shen, Y.Y.; Li, H. Composition effect in CuZr nanoparticles for CO₂ conversion to CH₃OH. *Mater. Chem. Phys.* **2022**, *283*, 125994. [[CrossRef](#)]
114. Hu, R.; Wang, T.; Li, H.; Zhu, Y.; Wang, Y.; Wen, F.; Xing, E.; Wu, Y.; Da, Z. Cu and Cu-Fe Bi-Metal Nanoparticles Encapsulated in Hollow S⁻¹ Zeolite for Reverse Water Gas Shift Reaction. *Catalysts* **2023**, *13*, 1037. [[CrossRef](#)]
115. Gao, Y.; Xiong, K.; Zhu, B. Design of Cu/MoO_x for CO₂ Reduction via Reverse Water Gas Shift Reaction. *Catalysts* **2023**, *13*, 684. [[CrossRef](#)]
116. Tarifa, P.; González-Castaño, M.; Cazaña, F.; Monzón, A.; Arellano-García, H. Development of one-pot Cu/cellulose derived carbon catalysts for RWGS reaction. *Fuel* **2022**, *319*, 123707. [[CrossRef](#)]
117. Zuo, J.; Na, W.; Zhang, P.; Yang, X.; Wen, J.; Zheng, M.; Wang, H. Enhanced activity of Ce_xZr_{1-x}O₂ solid solutions supported Cu-based catalysts for hydrogenation of CO₂ to methanol. *Mol. Catal.* **2022**, *526*, 112357. [[CrossRef](#)]
118. Hu, M.; Hu, H.; Tang, S.; Pan, Z. Enhanced CuAl₂O₄ Catalytic Activity via Alkalinization Treatment toward High CO₂ Conversion during Reverse Water Gas Shift Reaction. *Catalysts* **2022**, *12*, 1511. [[CrossRef](#)]
119. Cui, X.; Liu, Y.; Yan, W.; Xue, Y.; Mei, Y.; Li, J.; Gao, X.; Zhang, H.; Zhu, S.; Niu, Y.; et al. Enhancing methanol selectivity of commercial Cu/ZnO/Al₂O₃ catalyst in CO₂ hydrogenation by surface silylation. *Appl. Catal. B-Environ.* **2023**, *339*, 123099. [[CrossRef](#)]
120. Querido, A.R.; Goncalves, L.P.L.; Kolen'ko, Y.V.; Pereira, M.F.R.; Soares, O.S.G.P. Enhancing the performance of Cu catalysts for the reverse water-gas shift reaction using N-doped CNT-ZnO composite as support. *Catal. Sci. Technol.* **2023**, *13*, 3606. [[CrossRef](#)]

121. Pahija, E.; Panaritis, C.; Rutherford, B.; Couillard, M.; Patarachao, B.; Shadbahr, J.; Bensebaa, F.; Patience, G.S.; Boffito, D.C. FeO_x nanoparticle doping on Cu/Al₂O₃ catalysts for the reverse water gas shift. *J. CO₂ Util.* **2022**, *64*, 102155. [[CrossRef](#)]
122. Wang, J.; Couillard, M.; Baranova, E.A. Insight into Electrochemical Promotion of Cu/Co₃O₄ Catalysts for the Reverse Water Gas Shift Reaction. *ChemCatChem* **2023**, *15*, e202201514. [[CrossRef](#)]
123. Álvarez-Hernández, D.; Marín-Sánchez, M.; Lobo-Andrades, L.; Azancot, L.; Bobadilla, L.F.; Ivanova, S.; Centeno, M.A. Low-temperature reverse water gas-shift reaction over highly efficient Cu-hydrotalcites: Mechanistic insights on the role of malachite phase. *Catal. Today* **2023**, *422*, 114235. [[CrossRef](#)]
124. Liu, L.; Wang, X.; Lu, S.; Li, J.; Zhang, H.; Su, X.; Xue, F.; Cao, B.; Fang, T. Mechanism of CO₂ hydrogenation over a Zr₁-Cu single-atom catalyst. *New J. Chem.* **2022**, *11*, 5043–5051. [[CrossRef](#)]
125. Chen, Q.; Chen, X.; Ke, Q. Mechanism of CO₂ hydrogenation to methanol on the W-doped Rh(111) surface unveiled by first-principles calculation. *Colloids Surf. A* **2022**, *638*, 128332. [[CrossRef](#)]
126. Jurado, A.; Morales-García, A.; Viñes, F.; Illas, F. Molecular Mechanism and Microkinetic Analysis of the Reverse Water Gas Shift Reaction Heterogeneously Catalyzed by the Mo₂C MXene. *ACS Catal.* **2022**, *12*, 15658. [[CrossRef](#)]
127. Ortner, N.; Zhao, D.; Mena, H.; Weiß, J.; Lund, H.; Bartling, S.; Wohlrab, S.; Armbruster, U.; Kondratenko, E.V. Revealing Origins of Methanol Selectivity Loss in CO₂ Hydrogenation over CuZn-Containing Catalysts. *ACS Catal.* **2023**, *13*, 60. [[CrossRef](#)]
128. Phey, M.L.P.; Abdullah, T.A.T.; Ali, U.F.M.; Mohamud, M.Y.; Ikram, M.; Nabgan, W. Reverse water gas shift reaction over a Cu/ZnO catalyst supported on regenerated spent bleaching earth (RSBE) in a slurry reactor: The effect of the Cu/Zn ratio on the catalytic activity. *RSC Adv.* **2023**, *5*, 3039. [[CrossRef](#)]
129. Zhang, W.; Vidal-López, A.; Comas-Vives, A. Theoretical study of the catalytic performance of Fe and Cu single-atom catalysts supported on Mo₂C toward the reverse water-gas shift reaction. *Front. Chem.* **2023**, *11*, 1144189. [[CrossRef](#)] [[PubMed](#)]
130. Zafar, F.; Zhao, R.; Ali, M.; Park, Y.M.; Roh, H.; Gao, X.; Tian, J.; Bae, J.W. Unprecedented contributions of In₂O₃ promoter on ordered mesoporous Cu/Al₂O₃ for CO₂ hydrogenation to oxygenates. *Chem. Eng. J.* **2022**, *439*, 135649. [[CrossRef](#)]
131. Li, Y.; Chen, D.; Fang, Z.; Zhou, H.; Zhu, J.; Li, Y.; Huang, S.; Lin, W.; Zhang, Y. Unveiling the role of adsorbed hydrogen in tuning the catalytic activity of CO₂ conversion to methanol at Cu/TiC surfaces. *J. CO₂ Util.* **2023**, *72*, 102515. [[CrossRef](#)]
132. Chen, W.; Maugé, F.; Van Gestel, J.; Nie, H.; Li, D.; Long, X. Effect of modification of the alumina acidity on the properties of supported Mo and CoMo sulfide catalysts. *J. Cat.* **2013**, *304*, 47. [[CrossRef](#)]
133. Sameer, S.; Singh, G.; Gahtori, J.; Goyal, R.; Ghosh, I.K.; Barrabes, N.; Bordoloi, A. Molybdenum sulfide embedded mesoporous N-Doped carbon as a noble metal-free highly selective catalyst for conversion of CO₂ to CO. *J. Environ. Chem. Eng.* **2022**, *10*, 108988. [[CrossRef](#)]
134. Zhang, J.; Feng, K.; Li, Z.; Yang, B.; Yan, B.; Luo, K.H. Defect-Driven Efficient Selective CO₂ Hydrogenation with Mo-Based Clusters. *JACS Au.* **2023**, *3*, 2736. [[CrossRef](#)] [[PubMed](#)]
135. Dasireddy, V.D.B.C.; Vengust, D.; Likozar, B.; Kovač, J.; Mrzel, A. Production of syngas by CO₂ reduction through reverse water gas shift (RWGS) over catalytically active molybdenum based carbide, nitride and composite nanowires. *Renew. Energy* **2021**, *176*, 251. [[CrossRef](#)]
136. Xin, H.; Lin, L.; Li, R.; Li, D.; Song, T.Y.; Mu, R.T.; Fu, Q.; Bao, X.H. Overtuning CO₂ hydrogenation selectivity with high activity via reaction induced strong metal support Interactions. *J. Am. Chem. Soc.* **2022**, *144*, 4874. [[CrossRef](#)]
137. Zhang, Q.; Pastor-Pérez, L.; Jin, W.; Gu, S.; Reina, T.R. Understanding the promoter effect of Cu and Cs over highly effective β-Mo₂C catalysts for the reverse water-gas shift reaction. *Appl. Catal. B-Env.* **2019**, *244*, 889. [[CrossRef](#)]
138. Zhang, Q.; Bown, M.; Pastor-Pérez, L.; Duyar, M.S.; Reina, T.R. CO₂ Conversion via Reverse Water Gas Shift Reaction Using Fully Selective Mo-P Multicomponent Catalysts. *Ind. Eng. Chem. Res.* **2022**, *61*, 12857. [[CrossRef](#)]
139. Yuan, Y.; Qi, L.; Gao, Z.; Guo, T.; Zhai, D.; He, Y.; Ma, J.; Guo, Q. Performance Exploration of Ni-Doped MoS₂ in CO₂ Hydrogenation to Methanol. *Molecules* **2023**, *28*, 5796. [[CrossRef](#)]
140. Pajares, A.; Prats, H.; Romero, A.; Viñes, F.; Piscina, P.R.; Sayós, R.; Homs, N.; Illas, F. Critical effect of carbon vacancies on the reverse water gas shift reaction over vanadium carbide catalysts. *Appl. Catal. B-Environ.* **2020**, *267*, 118719. [[CrossRef](#)]
141. Morse, J.R.; Juneau, M.; Baldwin, J.W.; Porosoff, M.D.; Willauer, H.D. Alkali promoted tungsten carbide as a selective catalyst for the reverse water gas shift reaction. *J. CO₂ Util.* **2020**, *35*, 38. [[CrossRef](#)]
142. Juneau, M.; Yaffe, D.; Liu, R.; Agwara, J.N.; Porosoff, M.D. Establishing tungsten carbides as active catalysts for CO₂ Hydrogenation. *Nanoscale* **2022**, *14*, 16458. [[CrossRef](#)] [[PubMed](#)]
143. Zhang, S.; Liu, X.; Luo, H.; Wu, Z.; Wei, B.; Shao, Z.; Huang, C.; Hua, K.; Xia, L.; Li, J.; et al. Morphological Modulation of Co₂C by Surface-Adsorbed Species for Highly Effective Low-Temperature CO₂ Reduction. *ACS Catal.* **2022**, *12*, 8544–8557. [[CrossRef](#)]
144. Reddy, K.P.; Dama, S.; Mhamane, N.B.; Ghosalya, M.K.; Raja, T.; Satyanarayana, C.V.; Gopinath, C.S. Molybdenum carbide catalyst for the reduction of CO₂ to CO: Surface science aspects by nappes and catalysis studies. *Dalton Trans.* **2019**, *48*, 12199. [[CrossRef](#)]
145. Marquart, W.; Raseale, S.; Prieto, G.; Zimina, A.; Fisher, N. CO₂ reduction over Mo₂C-based catalysts. *ACS Catal.* **2021**, *11*, 1624. [[CrossRef](#)]
146. Holder, C.F.; Morse, J.R.; Barboun, P.M.; Shabaev, A.R.; Baldwin, J.W.; Willauer, H.D. Evaluating metal oxide support effects on the RWGS activity of Mo₂C catalysts. *Catal. Sci. Technol.* **2023**, *13*, 2685. [[CrossRef](#)]
147. Pajares, A.; Liu, X.; Busacker, J.R.; Piscina, P.R.D.L.; Homs, N. Supported Nanostructured Mo_xC Materials for the Catalytic Reduction of CO₂ through the Reverse Water Gas Shift Reaction. *Nanomaterials* **2022**, *12*, 3165. [[CrossRef](#)] [[PubMed](#)]

148. Ortega-Trigueros, A.; Caccia, M.; Caccia, J. Tuning Activity and Selectivity in Catalyzed Reactions of Environmental and Industrial Importance with a High-Surface Area, Mesoporous Mo₂C Catalyst. *Chem. Mater.* **2022**, *34*, 6232. [[CrossRef](#)]
149. Liu, R.; Chen, C.; Chu, W.; Sun, W. Unveiling the Origin of Alkali Metal (Na, K, Rb, and Cs) Promotion in CO₂ Dissociation over Mo₂C Catalysts. *Materials* **2022**, *15*, 3775. [[CrossRef](#)]
150. Bhavani, A.G.; Kim, W.Y.; Lee, J.S. Barium substituted lanthanum manganite perovskite for CO₂ reforming of methane. *ACS Catal* **2013**, *3*, 1537. [[CrossRef](#)]
151. Royer, S.; Alamdari, H.; Duprez, D.; Kaliaguine, S. Oxygen storage capacity of La_{1-x}A'BO₃ perovskites (with A'=Sr, Ce; B=Co, Mn) relation with catalytic activity in the CH₄ oxidation reaction. *Appl. Catal. B Environ.* **2005**, *58*, 273. [[CrossRef](#)]
152. Kim, D.H.; Park, J.L.; Park, E.J.; Kim, Y.D.; Uhm, S. Dopant effect of barium zirconate-based perovskite-type catalysts for the intermediate temperature reverse water gas shift reaction. *ACS Catal.* **2014**, *4*, 3117. [[CrossRef](#)]
153. Jo, A.; Kim, Y.; Lim, H.S.; Lee, M.; Kang, D.; Lee, J.W. Controlled template removal from nanocast La_{0.8}Sr_{0.2}FeO₃ for enhanced CO₂ conversion by reverse water gas shift chemical looping. *J. CO₂ Util.* **2022**, *56*, 101845. [[CrossRef](#)]
154. Yu, J.; Muhetaer, A.; Gao, X.; Zhang, Z.; Yang, Y.; Li, Q.; Chen, L.; Liu, H.; Xu, D. Highly Active Hydrogen-rich Photothermal Reverse Water Gas Shift Reaction on Ni/LaInO₃ Perovskite Catalysts with Near-unity Selectivity. *Angew. Chem. Int. Ed.* **2023**, *62*, e202303135. [[CrossRef](#)] [[PubMed](#)]
155. Kopac, D.; Likozar, B.; Hus, M. How size matters: Electronic, cooperative, and geometric effect in perovskite supported copper catalysts for CO₂ reduction. *ACS Catal.* **2020**, *10*, 4102. [[CrossRef](#)]
156. Chen, Y.; Hong, H.F.; Cai, J.Y.; Li, Z. Highly Efficient CO₂ to CO transformation over Cu-based catalyst derived from a CuMgAl-Layered Double Hydroxide (LDH). *ChemCatChem* **2021**, *13*, 656. [[CrossRef](#)]
157. Goguet, A.; Meunier, F.C.; Tibiletti, D.; Breen, J.P.; Burch, R. Spectrokinetic investigation of reverse water gas shift reaction Intermediates over a Pt/CeO₂ Catalyst. *J. Phys. Chem. B* **2004**, *108*, 20240. [[CrossRef](#)]

Disclaimer/Publisher's Note: The statements, opinions and data contained in all publications are solely those of the individual author(s) and contributor(s) and not of MDPI and/or the editor(s). MDPI and/or the editor(s) disclaim responsibility for any injury to people or property resulting from any ideas, methods, instructions or products referred to in the content.